Comprehensive defect suppression in perovskite nanocrystals for high-efficiency light-emitting diodes

Young-Hoon Kim[1,2†], Sungjin Kim[1,2†], Arvin Kakekhani[3†], Jinwoo Park[1,2], Jaehyeok Park[4], Sung Heo[5], Yong-Hee Lee[1], Hengxing Xu[6], Satyawan Nagane[7], Dongwook Lee[5], Robert B. Wexler[3], Dong-Hyeok Kim[1,2], Seung Hyeon Jo[1,2], Laura Martínez-Sarti[8], Peng Tan[3,9], Aditya Sadhanala[7,10], Gyeong-Su Park[1], Young-Woon Kim[1], Bin-Hu[6], Henk J. Bolink[8], Seunghyup Yoo[4], Richard H. Friend[7], Andrew M. Rappe[3*], and Tae-Woo Lee[1,2*]

[1]Department of Materials Science and Engineering, Seoul National University, 1 Gwanak-ro, Gwanak-gu, Seoul 08826, Republic of Korea

[2]School of Chemical and Biological Engineering, Institute of Engineering Research, Research Institute of Advanced Materials, Nano Systems Institute (NSI), Seoul National University, 1 Gwanak-ro, Gwanak-gu, Seoul 08826, Republic of Korea

[3]Department of Chemistry, University of Pennsylvania, Philadelphia, Pennsylvania 19104, USA

[4]School of Electrical Engineering, Korea Advanced Institute of Science and Technology (KAIST), Daejeon 34141, Republic of Korea.

[5]Group for Molecular Engineering of Functional Materials, Ecole Polytechnique Fédérale de Lausanne, CH-1951 Sion, Switzerland

[6]Department of Materials Science and Engineering, University of Tennessee, Knoxville, TN 37996, USA

[7]Cavendish Laboratory, University of Cambridge, JJ Thomson Avenue, Cambridge CB3 0HE, U.K.

[8]Instituto de Ciencia Molecular (ICMol), Universidad de Valencia, Catedrático José Beltrán, 2, 46980 Paterna, Spain

[9]Department of Physics, Harbin Institute of Technology, Harbin 150001, China

[10]Clarendon Laboratory, Department of Physics, University of Oxford, Parks Road, Oxford OX1 3PU, UK.

† *These authors contributed equally to this work.*

**Authors to whom correspondence should be addressed: E-mail: twlees@snu.ac.kr, taewlees@gmail.com, rappe@sas.upenn.edu*

Electroluminescence efficiencies of metal halide perovskite nanocrystals (PNCs) are limited by lack of material strategies that can both suppress formation of defects and enhance charge carrier confinement. Here, we report a one-dopant alloying strategy that generates smaller, monodisperse colloidal particles (confining electrons and holes and boosting radiative recombination) with fewer surface defects (reducing nonradiative recombination). Doping of guanidinium (GA) into formamidinium lead bromide PNCs yields limited bulk solubility while creating an entropy-stabilized phase in the PNCs and leading to smaller PNCs with more carrier confinement. The extra GA segregates to the surface and stabilizes the under-coordinated sites. Additionally, a surface stabilizing 1,3,5-tris(bromomethyl)-2,4,6-triethylbenzene was applied as a Br vacancy healing agent. The result is highly efficient PNC-based light-emitting diodes that have current efficiency of 108 cd·A^{-1} (external quantum efficiency (EQE) of 23.4 %) which rises to 205 cd·A^{-1} (EQE of 45.5 %) with a hemispherical lens.

Metal halide perovskites (MHPs) with the general ABX_3 formula (A = organic or inorganic cation, B = metal cation, X = halide anion) have narrow emission spectra (full width at half maximum ≈ 20 nm) that can achieve high color-purity, tunable emission wavelength range (400 nm ≤ λ ≤ 780 nm) and low-cost solution processability[1–6]. As a result, they have been regarded as promising light emitters[5–12]. This has also led to perovskite light-emitting diodes (PeLEDs), which have shown a tremendous increase in electroluminescence (EL) efficiencies[13–15]. These improvements have been obtained by a) increasing radiative recombination rate[16], and b) lowering non-radiative recombination rate[17]. The radiative recombination rate of the charge carriers has been increased by spatially confining the electrons and holes in small perovskite polycrystalline nano-grains[3], low-dimensional crystals[18–20], or colloidal perovskite nanocrystals (PNCs)[4,5]. To reach beyond the state of the art and further increase the EL efficiency, more effective strategies for suppression of defects and associated non-radiative

recombination are required.

In perovskite polycrystalline bulk films, stoichiometry control of precursors[3], use of passivation agents[18–21] and post-treatments[14,22,23] were shown to lead to the highest current efficiency (CE) = 78 $cd \cdot A^{-1}$ (external quantum efficiency (EQE) of 20.3% ph/el based on Lambertian assumption)[18]. In colloidal PNCs, non-radiative recombination and defects are reduced by surface-binding ligands. However, this method has limitations: a) the dynamic nature of ligand-surface bonds, and b) steric hindrance effects that can leave under-coordinated sites unpassivated and prone to defect formation[8,9]. B-site cation engineering[10], X-site anion exchange[11], and surface-binding ligand engineering[12] have also been used, leading to the highest CE of 76.8 $cd \cdot A^{-1}$ (EQE of 17.1% ph/el) in green emission[24] and CE of 10.6 $cd \cdot A^{-1}$ (EQE of 21.3% ph/el considering angular EL distribution) in red emission[11] in PeLEDs based on $CsPbX_3$.

The majority of research on PeLEDs is based on all-inorganic PNCs. It has been shown that the orientational freedom of the liquid-like dipoles associated with the organic cations can reduce the charge recombination rates[25–28]. While beneficial for photovoltaic applications, this is undesirable for LEDs[29]. The all-inorganic MHPs contain spherical atomic A-site cations with zero dipole moment, leading to enhancement of charge-recombination. Nevertheless, there are shortcomings associated with the atomic A-site cations: a small phase space for tunability and a lack of lattice-stabilizing directional hydrogen bonds. At the same time, there has been lacking in comprehensive material design strategy to passivate the surface defects and confine charge carriers inside the nanocrystals.

Here, we propose a simple and rational PNC design to stabilize the under-coordinated sites at the surface and improve the charge carriers' confinement inside the nanocrystals simultaneously by employing zero-dipole guanidinium cation ($CH_6N_3^+$; GA^+)[30,31] that provides lattice-stabilizing effect of hydrogen bonds. We exploit fine substitutional doping of

formamidinium ($CH_5N_2^+$; FA^+) lead bromide ($FAPbBr_3$) by single GA^+ cation in colloidal PNCs instead of cation alloying approaches in perovskite polycrystalline bulk films that have been used in solar cells[32,33]. The increased surface stability is driven by the extra amino group in the GA^+ due to its extra hydrogen bonds[34] and more uniformly distributed positive charge[35]. Decylamine and oleic acid are also used as surface-binding ligands (Fig. 1a), providing an additional level of surface stabilization. We show that although from an internal energy point of view adding GA to the particle is penalized due to its larger size, the gain in configurational entropy[36] stabilizes low concentrations of GA. We further reduce non-radiative recombination by applying 1,3,5-tris(bromomethyl)-2,4,6-triethylbenzene (TBTB) overcoat, which can heal the leftover halide vacancies. Ultimately, we achieved a CE of 108 $cd \cdot A^{-1}$, further increased to 205 $cd \cdot A^{-1}$ by employing a hemispherical lens.

Results

Structural properties

We begin by studying how GA doping influences the $FAPbBr_3$ structure. We construct a computational model of $FAPbBr_3$ PNCs (see Supplementary Fig. 1 and Methods for details). The fully *ab-initio* extended bulk model (Fig. 1b) can represent the $FAPbBr_3$ PNCs and reproduce their experimental X-ray diffraction (XRD) patterns (Fig. 1c). We calculate the formation free energy (from precursors) of $FA_{1-x}GA_xPbBr_3$ as x increases from 0 to 1, taking into account both enthalpic and configurational entropic contributions (Fig. 1d). GA is larger than FA and beyond the tolerance of the (lead bromide based) perovskite structure[37–39], so enthalpy does not preferentially drive GA to the inside of the perovskite. Nonetheless, small concentrations (≈12.5%) of GA can still be dissolved in the structure due to entropy stabilization[36]. Beyond ≈12.5%, enthalpy wins over the entropy and drives the surplus GA to

the surface of the PNCs.

As *x* is increased from 0 to 1, the size of $FA_{1-x}GA_xPbBr_3$ PNCs decreases from ≈10 nm to ≈5.1 nm (Fig. 2a and Supplementary Fig. 2). The decrease in size is also confirmed by observing a general trend for relative increase of peak intensity ratio (of the organic ligands to inorganic perovskite components) in the X-ray photoelectron spectroscopy (XPS) measurements (see Supplementary Fig. 3 and associated discussion for more details). Increasing the GA concentration increases the enthalpy of the bulk of the PNCs, thereby destabilizing them. To compensate for this energy penalty, the PNCs increase their surface-to-bulk ratio by decreasing their size. The PNCs are stabilized by the surrounding acid/amine ligands. In samples that lack GA, the optimal surface-to-bulk ratio is determined by the balance between surface formation energy cost and the stabilization imparted by surface-binding ligands. As can be seen in Fig. 2b, c, the latter is a result of both chemical point interactions and dispersion interactions (involving alkyl and alkenyl groups). The point interactions involve the acid -COOH or amine $-NH_2$ groups and consist of both lone-pair interactions (accompanied by lone-pair polarization)[35,40] and hydrogen bonds. GA alters this balance and drives a tendency to increase the surface-to-bulk ratio, leading to an increased charge carrier confinement without inducing more defects on the PNC surfaces (as explained in the next section).

Our DFT calculations indicate that beyond low concentrations of GA, these cations have an energetic preference to migrate to the surface (Fig. 2d). As the GA concentration increases, the increase in the surface-to-bulk ratio ensures the presence of enough surface sites, at which most of the GA cations can reside (Supplementary Table 1). The inference that GA can only be incorporated into the bulk of the perovskite in low concentrations is supported by the GA-concentration dependent bulk moduli (calculated via elastic constants using the *ab-initio* stress-strain methodology), showing a sudden softening at higher GA concentrations (see Supplementary Fig. 4 and Supplementary Discussion 1 for more details). On the surface, the

cages formed by the $PbBr_6$ octahedra are broken and lack a confining cap, so the GA can more favorably fit in the surface sites. The extra amino group can effectively stay above the surface and favorably interact with the surface Br^- groups (Fig. 2d).

The photoluminescence (PL) spectrum experiments corroborate these inferences. The PL spectrum of $FA_{0.95}GA_{0.05}PbBr_3$ PNCs (Fig. 2e, Supplementary Fig. 5a) is slightly red-shifted compared to that of $FAPbBr_3$ PNCs. This change confirms that small concentrations of GA incorporate into $FA_{1-x}GA_xPbBr_3$ crystals and expand the lattice. This is also confirmed by XRD patterns (Supplementary Fig. 6). With increasing x ($\geq$ 0.1), PL spectra of $FA_{1-x}GA_xPbBr_3$ gradually blue-shift, while the intensity of the XRD peaks drop due to the size decrease (Fig. 2f). At x > 0.6, the structure of the PNCs begins to change, first to an amorphous-like (or with low crystallinity) phase in which small core perovskite crystals are fully covered by GA and then to a non-perovskite guanidinium lead bromide phase (see the discussion below the Supplementary Table 1).

Defect suppression via GA doping

The surface GA population leads to effective defect passivation. The PLQE improves from 79.7% for $FAPbBr_3$ to 93.3% for $FA_{0.9}GA_{0.1}PbBr_3$ PNCs (in solution) (Fig. 3a). $FA_{0.9}GA_{0.1}PbBr_3$ PNC films also show a PLQE of 92.45% even without using core-shell structures both in film and solution. Defect suppression is directly confirmed by conducting deep-level transient spectroscopy (DLTS). Here, the device architecture includes an ITO/buffer hole-injection layer $(Buf\text{-}HIL)^2/FA_{1-x}GA_xPbBr_3$ PNCs (here, x=0, 0.1)/1,3,5-tris(N-phenyl benzimiazole-2-yl)benzene (TPBI)/LiF/Al (Fig. 3b). The DLTS spectrum shows a minimum at 250 K, which corresponds to a defect energy transition level of 0.3 to 0.4 eV. At x = 0.1, this signal attenuates, and the calculated defect density N_t declines from 4.93×10^{12} cm^{-3} to 3.10×10^{12} cm^{-3} (Supplementary Table 2).

GA doping extends the PL lifetime in $FA_{0.9}GA_{0.1}PbBr_3$ (≈113 ns), compared to $FAPbBr_3$ (≈88 ns) (Fig. 3c, Supplementary Fig. 5b). Our defect suppression scheme increases: a) the critical bias V_c as measured by the magneto-photocurrent in our PeLEDs (Supplementary Fig. 7a, b), b) the thermal stability as determined by thermogravimetric analysis (Supplementary Fig. 7c), c) the photo-stability with a smaller degree of attenuation in the shoulder of the PL spectrum peak at lower-energy states (Supplementary Fig. 7d-f), and d) the exciton binding energy as calculated from the temperature-dependent PL (Supplementary Fig. 7g-j and Supplementary Fig. 8).

GA stabilizes the PNC surfaces by increasing the number of H-bonds (as a result of the extra amino group relative to FA) with the under-coordinated surface Br^-. We have determined that the surface of the PNC has an AX-termination (see Supplementary Fig. 1 and Supplementary Discussion 2). We define a cohesive energy metric for the top surface AX layer (see Supplementary Discussion 2) and use it to evaluate the increase in GA-driven surface stability. The change in this quantity (relative to no-GA surfaces) is ≈-350 meV (per GA) for extended surfaces (as in the basal planes of large PNCs), and ≈-390 meV for the very small quantum dots (QDs) that we have directly modeled (Fig. 3d), due to greater under-coordination in these small QDs (for example in corners and edges) relative to extended surfaces. Here, a negative value for a change in cohesive energy means greater surface stabilization.

DFT simulations of surface-binding ligands reveal relatively strong point interactions (-0.6 to -0.7 eV) with the surface (Fig. 2b), accompanied by additional (chain-length-dependent) dispersion interactions (Fig. 2c). These interactions are the root of the surface-stabilizing effect of these ligands (see Methods for details). The GA doping slightly weakens the binding of these ligands (see Supplementary Fig. 9 and Methods, Supplementary Fig. 10 and associated discussion); this is another indication that incorporating GA stabilizes the surface internally

and decreases its reactivity toward external agents. At x = 0.1, the PNCs are relatively large (Fig. 2a), the GA induces both bulk and surface stabilization, and is uniformly distributed. Most of the surface is still covered by FA, and, because of steric hindrance, ligands can only bind to a limited number of surface sites, and thus selectively bind to FA-sites, unaffected by the added GA (Supplementary Table 1). The positive effect of 10% GA is due to increased surface stability, reduced defects and increased electron-hole confinement, in addition to the bulk entropy stabilization.

By increasing the GA content and the surface-to-bulk ratio, the bulk-stabilizing effect of GA attenuates; nevertheless, as the PNC surfaces become dominantly GA-terminated, its surface-stabilizing effect increases (Supplementary Table 1). Consequently, at x=0.6 (with fully GA-covered surface) the PNC still showed a high PLQE of 92.4% in solutions and 91.55% in films. At $x > 0.6$, the crystallinity of the sample decreased, the perovskite phase was destabilized, new diffraction peaks appeared, and the PLQE dropped (Fig. 2f and 3a). Such a departure from the perovskite structure, upon increasing GA content, is related to the tendency of guanidinium halide perovskites to crystalize in non-perovskite structures, previously addressed in the literature, for iodoplumbates[39]. Our calculations also confirm this for the bromoplumbates (see Supplementary Fig. 11 and Methods for details). Our PNC materials design strategy for LEDs can be extended to halide perovskites with other halides and cations, to showcase this: we have experimentally studied methylammonium lead bromide ($MAPbBr_3$) PNCs. About 10% GA can be incorporated into $MAPbBr_3$ crystals, inducing red-shifted PL. Beyond ≈10%, GA is driven to the surface and reduces the size of the PNCs, inducing blue-shifted PL (Supplementary Fig. 12). The GA leads to effective defect passivation and improved PLQE in $MAPbBr_3$ PNCs. To further indicate the novel effects induced by the doped GA cations on colloidal PNCs, we experimentally studied $FAPbBr_3$ PNCs with other types of organic cations such as butylammonium bromide, octylammonium bromide, benzylammonium bromide and

phenethylammonium bromide (Supplementary Fig. 13). As the content of these organic cations increases (> 0.2), the PNCs show limited improvement in PLQE (< 86%) and several different shoulder peaks in PL spectrum due to various sizes or compositions of crystals. These results indicate that GA, featuring only one extra amino group and mainly residing on the surface of the colloidal PNCs, is a well-controlled materials alloying concept. The doped GA can suppress both the bulk and surface defects, with minimal changes to the dimensionality and composition, and can simultaneously increase the radiative recombination of the colloidal PNCs.

The use of GA to passivate the defects in $MAPbI_3$-based polycrystalline bulk films for solar cells has been reported[32,33]. Some of the unique insight garnered in our work includes: (a) We synthesize colloidal PNCs rather than perovskite polycrystalline bulk films, thus the GA, in addition to passivating defects, simultaneously controls the PNCs' size and enhances the radiative recombination. (b) We understand why GA can be incorporated into the PNC in small concentrations (≈10%), above which it migrates to the surface outermost layer of PNC. (c) We illustrate competing enthalpic and entropic effects for GA incorporation in the bulk and show that such a mixed phase is entropy-stabilized.

Achieving highest LED efficiencies

The EL efficiency of our PeLEDs (structure: ITO/Buf-HIL/$FA_{1-x}GA_xPbBr_3$ PNCs/TPBI/ LiF/Al) increased from 61.3 to 95.7 $cd \cdot A^{-1}$ (Fig. 4), as x increased from 0 to 0.1. As x increases above 0.1, the current densities, luminance, and EL efficiencies of the PeLEDs gradually decrease; this trend can be ascribed to an increased ratio of insulating organic ligands surrounding the PNCs due to the increased surface-to-bulk ratio (Fig. 2a). The increased number of these insulating ligands hinders charge transport to the PNCs and thereby reduces the EL efficiency[41].

Our strategy was extended to further suppress surface defects and minimize non-radiative

recombination losses in the $FA_{0.9}GA_{0.1}PbBr_3$ PNC films by introducing a TBTB interlayer (≈5 nm) on the PNC films. TBTB interlayers between the PNC film and the TPBI layer can act as a Br vacancy healing agent and suppress surface defects in the PNC films. As can be seen in Fig. 5a, a TBTB molecule can readily deposit its Br into a surface Br-vacancy. The debrominated radical can then become hydrogenated in the environment containing acid ligands surrounding the PNCs and gets further stabilized (see Supplementary Discussion 2 for more details). These defect healing effects are confirmed by a decreased defect peak intensity and N_t in the DLTS measurements, by an increased PL lifetime, and by a blue-shifted PL spectrum (Supplementary Fig. 14a-c, Table 2). The insulating TBTB interlayers on the PNC films can also improve the charge balance in PeLEDs by retarding electron injection into emitting layers. This is confirmed by measuring the electron-current densities in electron-only devices (ITO/polyethylenimine ethoxylated (10 nm)/$FA_{0.9}GA_{0.1}PbBr_3$ PNCs with or without TBTB/TPBI/LiF/Al), by measuring hole-current densities in hole-only devices (ITO/Buf-HIL/$FA_{0.9}GA_{0.1}PbBr_3$ PNC films with or without TBTB/Tris(4-carbazoyl-9-ylphenyl)amine (50 nm)/MoO_3/Al) (Supplementary Fig. 14d, e). Additionally, capacitance-voltage characteristics in PeLEDs corroborates the delay in electron injection upon inserting the TBTB interlayer (Supplementary Fig. 14f). PeLEDs based on $FA_{0.9}GA_{0.1}PbBr_3$ PNCs and TBTB interlayers reach a maximum CE = 108 $cd \cdot A^{-1}$ and an external quantum efficiency (EQE) = 23.4%, calculated by using the full angular EL distribution (Fig. 5b-f). The distribution of CE obtained among 53 devices shows great reproducibility (Fig. 5g). We further improve the efficiency of our PeLEDs (to CE = 203 cd A^{-1} and EQE = 45.5 %), by placing a light out-coupling hemispherical lens on the emitting glass substrate. Optical simulations also verify that our devices without and with an out-coupling hemispherical lens can reach EQE = 30.2% and 55.61%, respectively (provided that the PLQE of PNC films is ≈1 and absorption loss of the

emitting layer is negligible) (Supplementary Fig. 15). These are the highest efficiencies yet reported among PeLEDs based on either polycrystalline bulk films or PNCs and surpass even the highest CE of conventional III-V and II-VI inorganic QD light-emitting diodes (LEDs) (Supplementary Fig. 16, Table 3,4). We also fabricated large-area PeLEDs (3 cm × 3 cm pixel) that used $FA_{0.9}GA_{0.1}PbBr_3$ PNCs (Fig. 5g inset) to demonstrate the promise of using hybrid colloidal PNCs in solid-state lighting devices and displays. PeLEDs based on $FA_{0.9}GA_{0.1}PbBr_3$ PNCs and TBTB interlayers showed a lifetime (when the initial luminance drops to 50 %) of 132 min (Fig. 6, Supplementary Fig. 17), which is improved by a factor of ≈8 relative to the previously reported highest-efficiency PeLEDs based on $FAPbBr_3$ PNCs[24].

Conclusions

We developed a comprehensive strategy that leads to a significant increase in the luminescence efficiency of perovskite nanocrystals (PNCs). This strategy makes it possible to simultaneously a) decrease the non-radiative charge recombination by comprehensive defect suppression and bulk entropy stabilization and b) increase the radiative recombination of charge carriers due to increased excitonic confinement. First, we used substitutional doping of GA into $FAPbBr_3$ PNCs to incorporate an optimal proportion of GA cations into the structure. The GA cations can reside in the bulk of the PNC in low concentrations (≈10%). The surplus GA then accumulates on the surface of the PNC. GA incorporation provides bulk-entropy stabilization, surface stabilization (by additional hydrogen bonding contributed by their extra amino group), and better electron-hole confinement. A GA to FA ratio of 0.1 was shown to maximize the EL efficiency. Moreover, 1,3,5-tris(bromomethyl)-2,4,6-triethylbenzene (TBTB) overcoats were introduced to heal the halide vacancy defects in $FA_{1-x}GA_xPbBr_3$ PNCs and to improve the charge balance in PeLEDs. These synergistic strategies yielded the highest EL

efficiencies in PNC-based PeLEDs (CE = 108 cd·A^{-1} and EQE = 23.4 %; CE = 203 cd·A^{-1} and EQE = 45.5 % with hemispherical lens). Our world-leading efficiencies demonstrate that this design strategy provides a clear pathway to translate PNCs into PeLEDs for a new generation of high-efficiency display applications.

References

1. Tan, Z.-K. *et al.* Bright light-emitting diodes based on organometal halide perovskite. *Nat. Nanotechnol.* **9**, 687–692 (2014).
2. Kim, Y.-H. *et al.* Multicolored organic/inorganic hybrid perovskite light-emitting diodes. *Adv. Mater.* **27**, 1248–1254 (2015).
3. Cho, H. *et al.* Overcoming the electroluminescence efficiency limitations of perovskite light-emitting diodes. *Science* **350**, 1222–1225 (2015).
4. Protesescu, L. *et al.* Nanocrystals of cesium lead halide perovskites ($CsPbX_3$, X = Cl, Br, and I): novel optoelectronic materials showing bright emission with wide color gamut. *Nano Lett.* **15**, 3692–3696 (2015).
5. Schmidt, L. C. *et al.* Nontemplate synthesis of $CH_3NH_3PbBr_3$ perovskite nanoparticles. *J. Am. Chem. Soc.* **136**, 850–853 (2014).
6. Kim, Y.-H., Cho, H. & Lee, T.-W. Metal halide perovskite light emitters. *Proc. Natl. Acad. Sci. U. S. A.* **113**, 11694–11702 (2016).
7. Kim, Y.-H., Kim, J. S. & Lee, T.-W. Strategies to improve luminescence efficiency of metal□halide perovskites and light□emitting diodes. *Adv. Mater.* **31**, 1804595 (2019).
8. Koscher, B. A., Swabeck, J. K., Bronstein, N. D. & Alivisatos, A. P. Essentially trap-free $CsPbBr_3$ colloidal nanocrystals by postsynthetic thiocyanate surface treatment. *J. Am. Chem. Soc.* **139**, 6566–6569 (2017).
9. De Roo, J. *et al.* Highly dynamic ligand binding and light absorption coefficient of cesium lead bromide perovskite nanocrystals. *ACS Nano* **10**, 2071–2081 (2016).
10. Wang, H.-C. *et al.* High-performance $CsPb_{1-x}Sn_xBr_3$ perovskite quantum dots for light-emitting diodes. *Angew. Chem. Int. Ed.* **56**, 13650–13654 (2017).
11. Chiba, T. *et al.* Anion-exchange red perovskite quantum dots with ammonium iodine salts for highly efficient light-emitting devices. *Nat. Photon.* **12**, 681–687 (2018).

12. Song, J. *et al.* Organic–inorganic hybrid passivation enables perovskite QLEDs with an EQE of 16.48%. *Adv. Mater.* **30**, 1805409 (2018).

13. Park, M.-H. *et al.* Boosting efficiency in polycrystalline metal halide perovskite light-emitting diodes. *ACS Energy Lett.* **4**, 1134–1149 (2019).

14. Xu, W. *et al.* Rational molecular passivation for high-performance perovskite light-emitting diodes. *Nat. Photon.* **13**, 418–424 (2019).

15. Zhao, X. & Tan, Z.-K. Large-area near-infrared perovskite light-emitting diodes. *Nat. Photon.* **14**, 215–218 (2020).

16. Yang, Y. *et al.* Comparison of recombination dynamics in $CH_3NH_3PbBr_3$ and $CH_3NH_3PbI_3$ perovskite films: influence of exciton binding energy. *J. Phys. Chem. Lett.* **6**, 4688–4692 (2015).

17. Stranks, S. D. *et al.* Recombination kinetics in organic-inorganic perovskites: excitons, free charge, and subgap states. *Phys. Rev. Appl.* **2**, 034007 (2014).

18. Lin, K. *et al.* Perovskite light-emitting diodes with external quantum efficiency exceeding 20 per cent. *Nature* **562**, 245–248 (2018).

19. Xiao, Z. *et al.* Efficient perovskite light-emitting diodes featuring nanometre-sized crystallites. *Nat. Photon.* **11**, 108–115 (2017).

20. Zhao, B. *et al.* High-efficiency perovskite–polymer bulk heterostructure light-emitting diodes. *Nat. Photon.* **12**, 783–789 (2018).

21. Cao, Y. *et al.* Perovskite light-emitting diodes based on spontaneously formed submicrometre-scale structures. *Nature* **562**, 249–253 (2018).

22. Yang, X. *et al.* Efficient green light-emitting diodes based on quasi-two-dimensional composition and phase engineered perovskite with surface passivation. *Nat. Commun.* **9**, 570 (2018).

23. Zhao, L. *et al.* Electrical stress influences the efficiency of $CH_3NH_3PbI_3$ perovskite light

emitting devices. *Adv. Mater.* **29**, 1605317 (2017).

24. Chen, H. *et al.* High-efficiency formamidinium lead bromide perovskite nanocrystal-based light-emitting diodes fabricated *via* a surface defect self□passivation strategy. *Adv. Opt. Mater.* **8**, 1901390 (2020).

25. Zhu, H. *et al.* Screening in crystalline liquids protects energetic carriers in hybrid perovskites. *Science* **353**, 1409–1413 (2016).

26. Yang, Y. *et al.* Observation of a hot-phonon bottleneck in lead-iodide perovskites. *Nat. Photon.* **10**, 53–59 (2016).

27. Zheng, F., Tan, L. Z., Liu, S. & Rappe, A. M. Rashba spin–orbit coupling enhanced carrier lifetime in $CH_3NH_3PbI_3$. *Nano Lett.* **15**, 7794–7800 (2015).

28. Rappe, A. M., Grinberg, I. & Spanier, J. E. Getting a charge out of hybrid perovskites. *Proc. Natl. Acad. Sci. U. S. A.* **114**, 7191–7193 (2017).

29. Swarnkar, A. *et al.* Quantum dot-induced phase stabilization of α-$CsPbI_3$ perovskite for high-efficiency photovoltaics. *Science* **354**, 92–95 (2016).

30. Banerjee, A., Chakraborty, S. & Ahuja, R. Bromination-induced stability enhancement with a multivalley optical response signature in guanidinium $[C(NH_2)_3]^+$-based hybrid perovskite solar cells. *J. Mater. Chem. A* **5**, 18561–18568 (2017).

31. Giorgi, G., Fujisawa, J.-I., Segawa, H. & Yamashita, K. Organic–inorganic hybrid lead iodide perovskite featuring zero dipole moment guanidinium cations: a theoretical analysis. *J. Phys. Chem. C* **119**, 4694–4701 (2015).

32. Jodlowski, A. D. *et al.* Large guanidinium cation mixed with methylammonium in lead iodide perovskites for 19% efficient solar cells. *Nat. Energy* **2**, 972–979 (2017).

33. Marco, N. D. *et al.* Guanidinium: a route to enhanced carrier lifetime and open-circuit voltage in hybrid perovskite solar cells. *Nano Lett.* **16**, 1009–1016 (2016).

34. Kanno, S., Imamura, Y. & Hada, M. First-principles calculations of the rotational motion

and hydrogen bond capability of large organic cations in hybrid perovskites. *J. Phys. Chem. C* **122**, 15966–15972 (2018).

35. Kakekhani, A., Katti, R. N. & Rappe, A. M. Water in hybrid perovskites: bulk $MAPbI_3$ degradation via super-hydrous state. *APL Mater.* **7**, 041112 (2019).

36. Yi, C. *et al.* Entropic stabilization of mixed A-cation ABX_3 metal halide perovskites for high performance perovskite solar cells. *Energy Environ. Sci.* **9**, 656–662 (2016).

37. Travis, W., Glover, E. N. K., Bronstein, H., Scanlon, D. O. & Palgrave, R. G. On the application of the tolerance factor to inorganic and hybrid halide perovskites: a revised system. *Chem. Sci.* **7**, 4548–4556 (2016).

38. Pham, N. D. *et al.* Tailoring crystal structure of $FA_{0.83}Cs_{0.17}PbI_3$ perovskite through guanidinium doping for enhanced performance and tunable hysteresis of planar perovskite solar cells. *Adv. Funct. Mater.* **29**, 1806479 (2019).

39. Deng, Z., Kieslich, G., Bristowe, P. D., Cheetham, A. K. & Sun, S. Octahedral connectivity and its role in determining the phase stabilities and electronic structures of low-dimensional, perovskite-related iodoplumbates. *APL Mater.* **6**, 114202 (2018).

40. Kakekhani, A. *et al.* Nature of lone-pair–surface bonds and their scaling relations. *Inorg. Chem.* **57**, 7222–7238 (2018).

41. Kim, Y.-H. *et al.* Highly efficient light-emitting diodes of colloidal metal–halide perovskite nanocrystals beyond quantum size. *ACS Nano* **11**, 6586–6593 (2017).

42. Contreras-García, J. *et al.* NCIPLOT: a program for plotting noncovalent interaction regions. *J. Chem. Theory Comput.* **7**, 625–632 (2011).

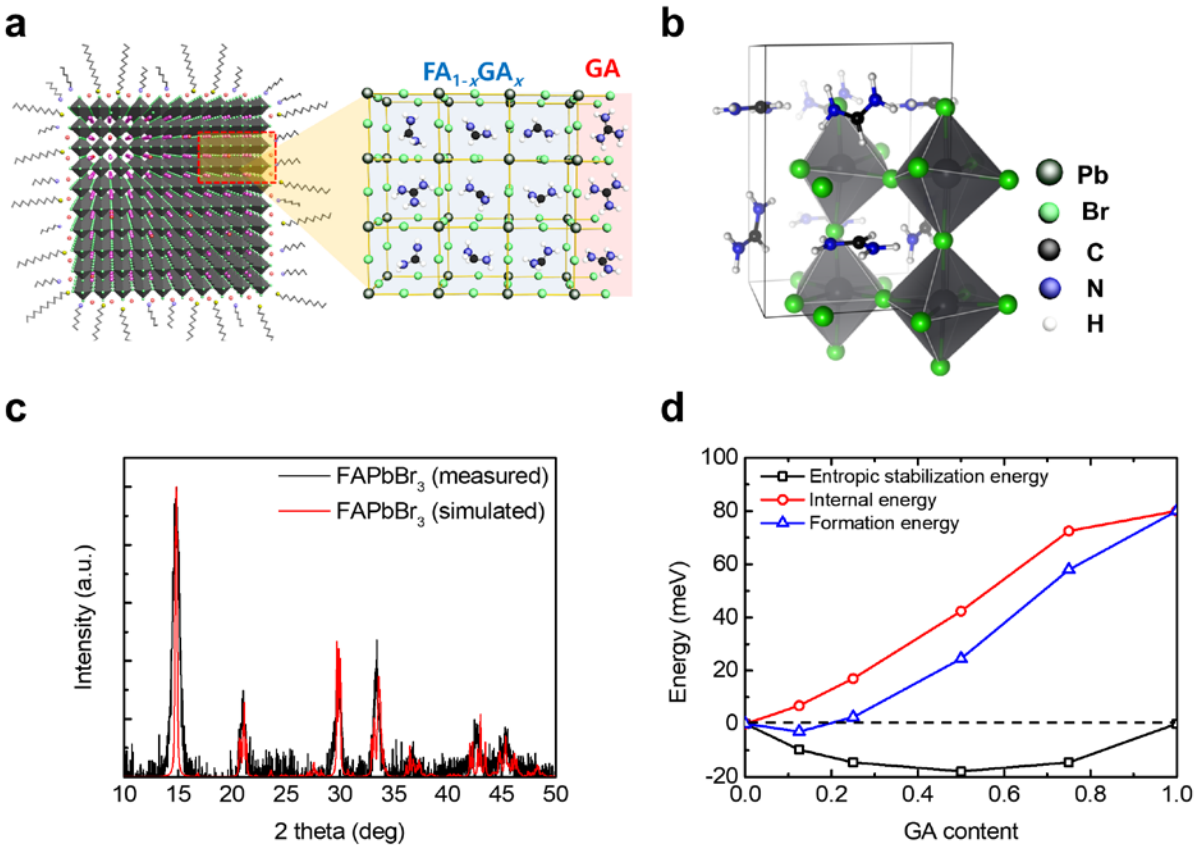

Fig. 1 | Structure of $FA_{1-x}GA_xPbBr_3$ PNCs. a, Schematic illustration of ligand-stabilized $FA_{1-x}GA_xPbBr_3$ PNC structure. **b,** Modeled bulk crystal structure of $FAPbBr_3$. **c,** Measured and DFT-simulated XRD patterns of $FAPbBr_3$. **d,** DFT formation energy (relative to the precursors), internal (enthalpic) energy and configurational entropic stabilization energy of $FA_{1-x}GA_xPbBr_3$ crystals ($0 \leq x \leq 1$).

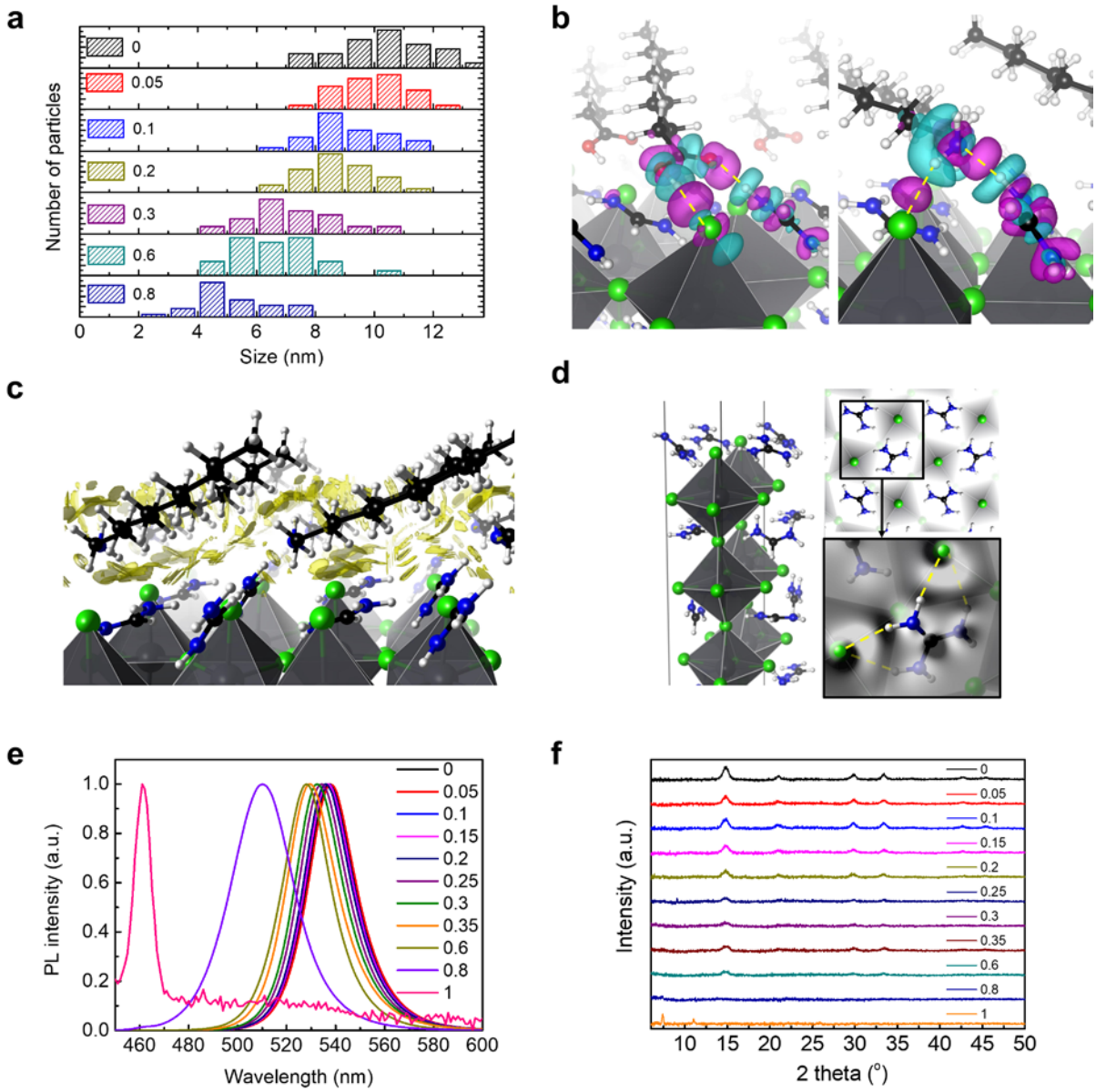

Fig. 2 | Structural and photophysical effects of GA on $FA_{1-x}GA_xPbBr_3$ PNCs. **a,** Experimentally-measured size distribution of $FA_{1-x}GA_xPbBr_3$ PNCs at $0 \leq x \leq 1$. **b,** 3D-Charge density difference (CDD) plots, showing the point chemical interactions between the perovskite surface and acid (left) or amine (right) ligands. The hydrogen and lone-pair bonds[35,40] can be noted by the magenta lobes along the yellow dashed lines. Cyan and magenta show regions of space that are depopulated or populated by electrons, respectively (as a result of the surface-ligand bonding). **c**, Yellow regions depict dispersion interactions among the

surface and surface-bound ligands. This is generated using the NCI (isovalue=0.6)[42]. **d,** Simulated crystal structure of GA-rich surface of $FA_{1-x}GA_xPbBr_3$ crystals in side view (left) and top view (top-right). At the bottom right, 2D-CDD plot (in gray scale), projected on the top Br layer plane, shows formation of hydrogen bonds between the GA and Br (white lobes along the yellow dashed lines). **e, f,** PL spectrum **(e)** and XRD patterns **(f)** of $FA_{1-x}GA_xPbBr_3$ PNCs at $0 \leq x \leq 1$.

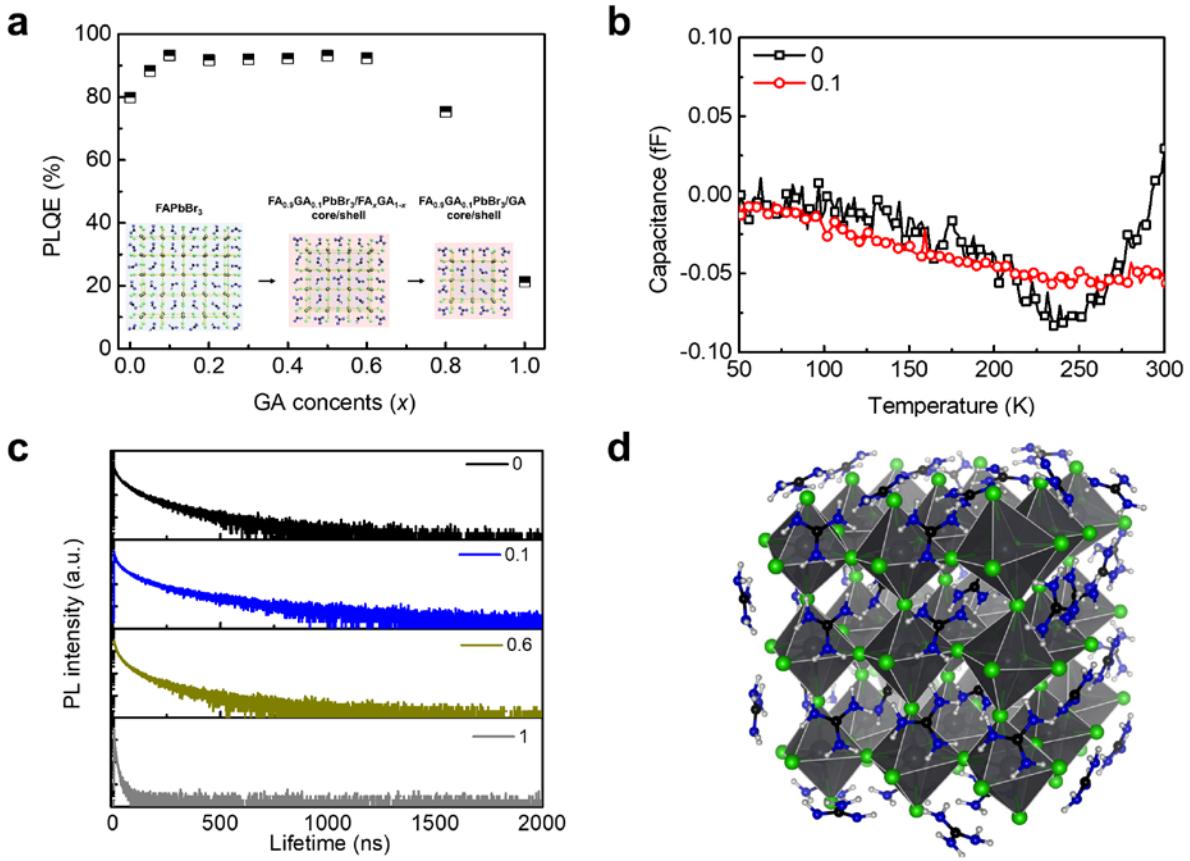

Fig. 3 | Defect analysis of $FA_{1-x}GA_xPbBr_3$ PNCs. a, PLQE and schematic crystal structures (inset) of $FA_{1-x}GA_xPbBr_3$ PNCs. **b,** DLTS data for PeLEDs based on $FA_{1-x}GA_xPbBr_3$ PNCs. **c,** PL lifetimes for $FA_{1-x}GA_xPbBr_3$ PNCs (x = 0, 0.1, 0.6, 1). **d,** A DFT-derived $FA_{1-x}GA_xPbBr_3$ quantum dot structure with GA shell and FA core.

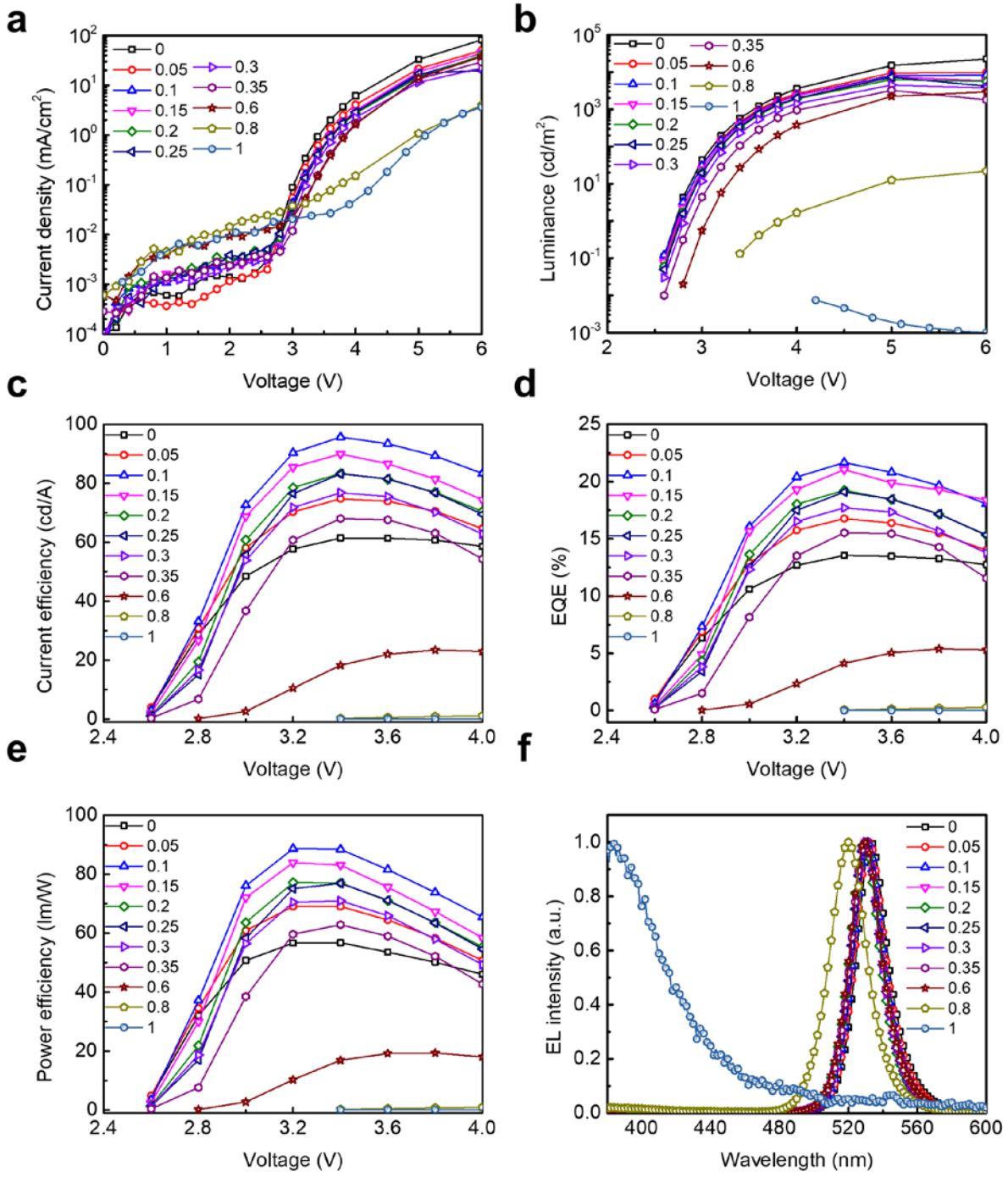

Fig. 4 | Characteristics of PeLEDs based on $FA_{1-x}GA_xPbBr_3$ PNCs. a-f, Current density **(a)**, luminance **(b)**, current efficiency **(c)**, external quantum efficiency **(d)**, power efficiency **(e)** and electroluminescence spectrum **(f)** of PeLEDs based on $FA_{1-x}GA_xPbBr_3$ PNCs ($0 \leq x \leq 1$).

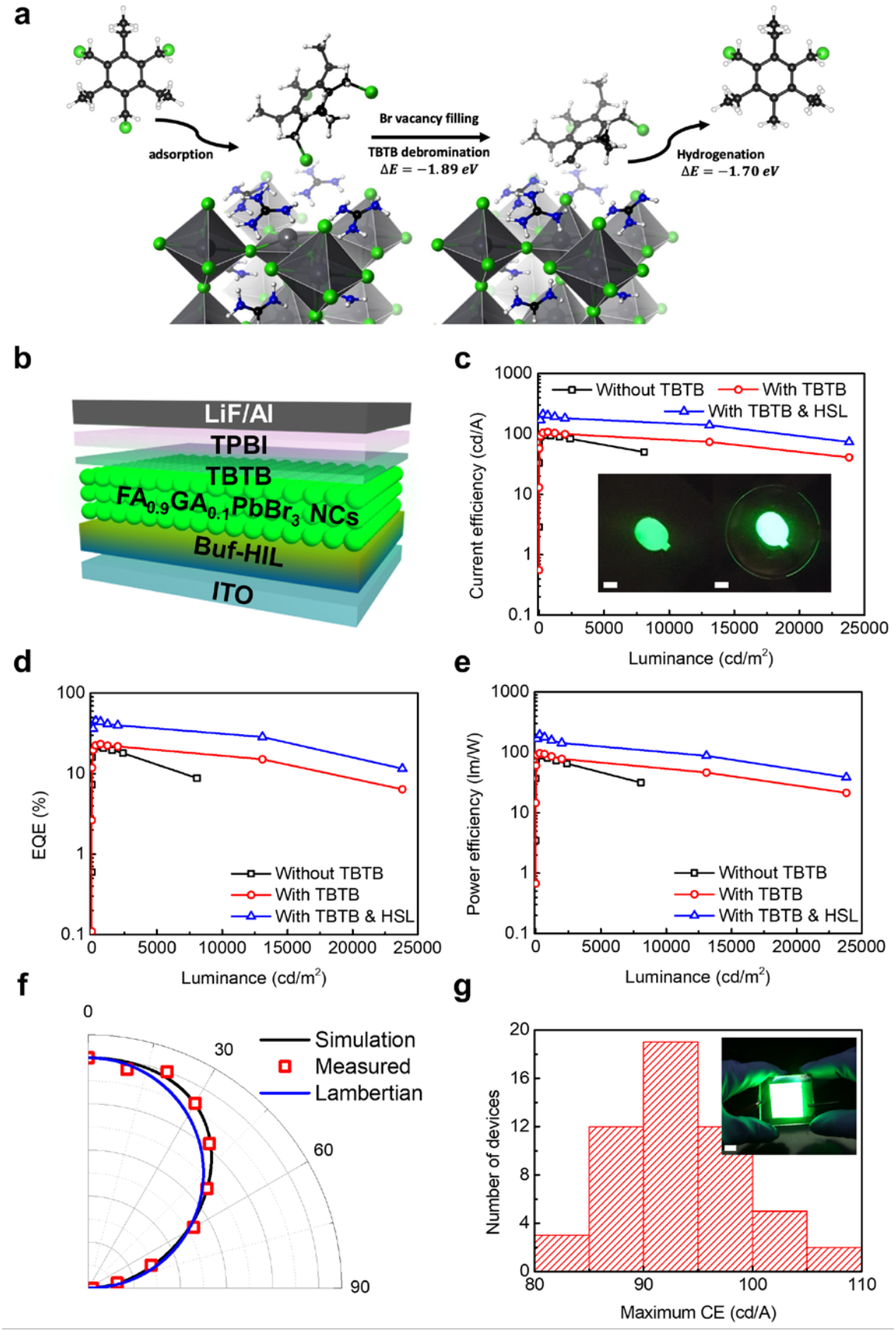
a
adsorption
Br vacancy filling
TBTB debromination
$\Delta E = -1.89\ eV$
Hydrogenation
$\Delta E = -1.70\ eV$
b
LiF/Al
TPBI
TBTB
$FA_{0.9}GA_{0.1}PbBr_3$ NCs
Buf-HIL
ITO
c
Without TBTB
With TBTB
With TBTB & HSL
Current efficiency (cd/A)
Luminance (cd/m^2)
d
EQE (%)
Without TBTB
With TBTB
With TBTB & HSL
Luminance (cd/m^2)
e
Power efficiency (lm/W)
Without TBTB
With TBTB
With TBTB & HSL
Luminance (cd/m^2)
f
Simulation
Measured
Lambertian
g
Number of devices
Maximum CE (cd/A)

Fig. 5 | Characteristics of PeLEDs with a TBTB interlayer. a, DFT-derived mechanism for Br-vacancy healing process driven by TBTB molecules on GA-terminated $FAPbBr_3$ surface. The debrominated radical can then achieve greater stability *via* further hydrogenation. The reaction energies (negative means exothermic) are shown by ΔE. **b,** Device structure of (x = 0.1) PeLEDs with TBTB interlayer. **c-e,** Current efficiency **(c)**, external quantum efficiency **(d)** and power efficiency **(e)** of PeLED devices (x=0.1) with/without a TBTB interlayer and a hemispherical lens. Inset: photographs of operating devices with TBTB, without (left) and with (right) a hemispherical lens (HSL) (scale bar: 1 mm). **f,** Angular intensity profiles for simulated emission, measured EL emission and Lambertian emission according to the viewing angles. **g,** Current efficiency histogram and photograph (inset, scale bar: 1 cm) of an operating large-area PeLEDs (3-cm by 3-cm pixel) with TBTB interlayer (x = 0.1).

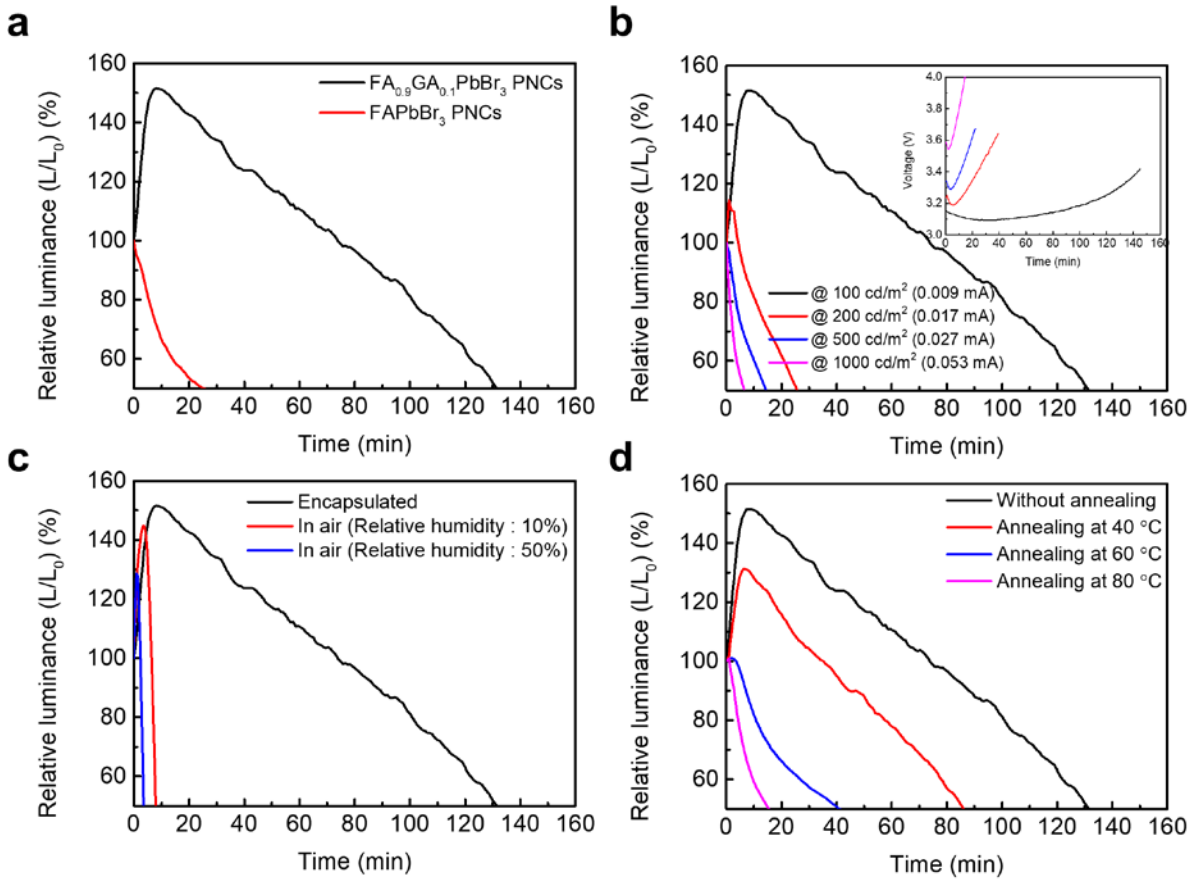

Fig. 6 | Device lifetime of PeLEDs. a, Device lifetime of PeLEDs based on $FA_{0.9}GA_{0.1}PbBr_3$ PNCs and $FAPbBr_3$ PNCs at an initial luminance of 100 cd/m^2. **b,** Device lifetime and operating voltage (inset) of PeLEDs based on $FA_{0.9}GA_{0.1}PbBr_3$ PNCs under different initial measurement luminance (applied current). **c,** Device lifetime of PeLEDs based on $FA_{0.9}GA_{0.1}PbBr_3$ PNCs at an initial luminance of 100 cd/m^2 under various environmental conditions. **d,** Device lifetime of PeLEDs based on $FA_{0.9}GA_{0.1}PbBr_3$ PNCs at an initial luminance of 100 cd/m^2 with different thermal annealing temperatures.

Methods

Synthesis of PNCs. All $FA_{1-x}GA_xPbBr_3$ PNCs were synthesized in air at room temperature. Precursor solutions were prepared by dissolving FABr (Dyesol Ltd.), GABr (Dyesol Ltd.) and $PbBr_2$ (Aldrich, 99.999%), with FABr:GABr ratio changing from 1:0 to 0:1, while maintaining the molarity of FABr:GABr at 0.1 mmol and the molarity of $PbBr_2$ at 0.2 mmol, in 0.5 mL of anhydrous *N*,*N*-dimethylformamide (DMF) (Aldrich, 99.8%). Then 0.15 mL of precursor solution dropped into a crystallization-inducing solution that is composed of 5 mL of toluene, 2 mL of 1-butanol, 0.3 mL of oleic acid and 0.02 mL of *n*-decylamine, then mixing for 10 min under vigorous stirring. The resulting colloidal PNCs were washed by sequential centrifugation and then collected in toluene.

PeLED fabrication & characterization. ITO patterned glasses were cleaned by sequential sonication in acetone and 2-isopropanol for 15 min each. The glasses were boiled in 2-isopropanol for 20 min, then transferred into an ultraviolet (UV)-ozone cleaner and treated with UV-ozone for 10 min to remove the residual organics. Then Buf-HILs composed of poly(3,4-ethylenedioxythiophene)/poly(styrene sulfonate) (PEDOT:PSS) and perfluorinated ionomer (PFI) were spin-coated in air to make a 40-nm thickness layer, then annealed at 150 °C for 30 min. Then the samples were transferred into a glove box, in which emitting layers were formed by spin-coating appropriate $FA_{1-x}GA_xPbBr_3$ PNC solutions at 1000 rpm for 60 s. The samples were transferred to a vacuum evaporator, then a 50-nm-thick layer of TPBI, a 1-nm-thick layer of LiF and a 100-nm-thick layer of Al were sequentially deposited. EL efficiencies of fabricated PeLEDs are measured using a Keithley 236 source measurement unit, and a Minolta CS 2000 spectroradiometer.

General information on our DFT simulations. We performed calculations using density functional theory (DFT) with plane wave basis sets using the Quantum Espresso software

package[43]. Ultrasoft GBRV pseudopotentials[44] and Perdew, Burke, Ernzerhof (PBE) exchange correlations (XC) have been used[45]. Dispersion interactions are accounted for using the Grimme DFT-D3 method[46]. The inclusion of dispersion interactions to accurately describe hybrid perovskite systems has been shown to be important[47]. As mentioned in the main text (in the context of Fig. 1c), the DFT-D3 dispersion correction can accurately describe the experimental data. We used a k-mesh sampling density greater than 15,000 points per $Å^{-3}$. The plane wave energy cutoff (Ecut) was chosen to be ≈550 eV, while the charge cutoff was chosen to be 10 times this value. We chose the force convergence criteria for the relaxation calculations to be very small, each force components on each atom has to be smaller than 10^{-4} Ry/au. Relative to the regular solid-state structures, we have molecular groups as part of the structure; consequently, the energy landscape can have regions with very small energy gradients (mostly corresponding to the rotations of the molecular groups), thus precise calculations of forces and low enough force convergence thresholds is necessary to properly exploring the real local minima of such structures. Most of our calculations (except some molecule in box calculations), are variable-cell relaxations (vc-relax), in which both the atomic coordinates and the cell vectors are optimized to find the zero-force, zero-stress structures with minimum internal energy. The smearing scheme for the Kohn−Sham orbitals' occupations is the cold smearing of Marzari and Vanderbilt[48] with a temperature equal to 10 mRy/kB. The computational XRD patterns were generated using the Mercury software[49], with fully-relaxed atomic coordinates and lattice constants as input. Using the aforementioned convergence parameters, we could successfully achieve the (≈1 meV per f.u.c.) precision we need in formation energy plots (Fig. 1d), and a virtually perfect structural agreement with experiment (Fig. 1c). To calculate the reduced density gradient and the NCI index[42] we used norm-conserving pseudopotentials, as opposed to ultrasoft ones. The ecut for these calculations were chosen to be ≈680 eV. The charge density differences calculations for ligands' binding were also performed using norm-

conserving pseudopotentials to be consistent with the NCI plots.

PL and PLQE measurement. PL spectra of $FA_{1-x}GA_xPbBr_3$ PNCs in solution states were measured using a JASCO FP8500 spectrofluorometer. PLQEs were detected by a 100-nm integrating sphere (ILF-835) that is mounted on the same spectrofluorometer, and calculated using Jasco SpectraManager II Software. The PLQE of the thin film samples was measured using an integrating sphere method. A continuous-wave 405-nm blue diode laser with an excitation power of 50 μW and a focused beam spot of ~0.3 mm^2 was used to photo-excite the samples. Emission was measured using an Andor iDus Silicon detector. The samples were encapsulated between two glass cover slips before measurements.

Time-correlated single-photon counting measurement (TCSPC). PL lifetimes of $FA_{1-x}GA_xPbBr_3$ PNCs were measured using a FluoTime 300. $FA_{1-x}GA_xPbBr_3$ PNCs were photo-excited by a picosecond-pulse laser head (excitation wavelength = 405 nm, LDH-P-C-405B, PicoQuant) and their PL lifetimes were detected using a photon-counting detector (PMA Hybrid 07) and a TCSPC module (PicoHarp, PicoQuant).

Transmission electron microscopy (TEM) Measurement. To measure TEM image of PNCs, 0.05 mL of $FA_{1-x}GA_xPbBr_3$ PNC solutions were dropped onto a Cu grid and TEM images were measured using a JEOL-JEM 2100F with an acceleration voltage of 200 kV.

Deep-level transient spectroscopy (DLTS). DLTS measurements were performed with a PhysTech FT1030 DLTS system. The capacitance was measured using a modified Boonton 72B capacitance meter with a 1 MHz capacitance meter. Temperature scans were made between 20 and 300 K, at a heating rate of 2 K/min. Samples were placed in the He-contact gas of a liquid helium cryostat. The pulse height, filling pulse width, and pulse period width are 0.4 V, 10 ms, and 10 ms, respectively. The activation energy, capture cross-section, and concentration

of traps were calculated using an Arrhenius plot.

DFT calculations of structures. In order to model the hybrid perovskite systems, we have studied in this work, we used fully vc-relaxed, self-consistent DFT-derived structure. This means no constraint is assumed and implemented on the atomic positions or lattice vectors. In hybrid perovskite materials, the higher temperatures derive the structures towards higher effective symmetries due to thermal and spatial averaging of the local structural symmetries. But as it has been recently pointed out by Zunger and co-workers, the nominal higher symmetry (cubic) perovskite structures deduced from X-Ray diffraction which are macroscopically averaged, should not be used to model the electronic properties (naturally including formation and binding energies), which are sensitive to the order and coordination of atoms in angstrom scale rather than a macroscopic average[50]. Formamidinium lead bromide ($FAPbBr_3$) is experimentally known to have a low temperature orthorhombic structure and a room temperature cubic phase. Both of these are actually an averaged order, and we find a, technically-speaking, triclinic structure to be the fully self-consistent DFT structure. This structure is greatly similar to the orthorhombic phase (only very small deviations in cell parameters from the ideal orthorhombic phase). This structure is depicted in Fig. 1b. The volume of such a structure is $\approx$852 Å^3, within $\approx$2% error of the experimentally-measured value for this phase. This corresponds to an error of $\approx$0.5 % in lattice constants. Moreover, as mentioned in the main text such structure is able to reproduce the experimental XRD patterns virtually perfectly (Fig. 1c). As it has been pointed out experimentally such a phase has c(2×2)×2 structure, in which the FA cations have an alternative orientational pattern i.e., the long direction of the molecule alternates its orientation (Fig. 1c). We also perform DFT calculations of surfaces and quantum dots, for more details see Supplementary Discussion 2.

DFT calculations of bulk energies. In order to calculate the internal and free energies reported

in Fig. 1d we perform the procedure that is explained here. For calculations regarding 0, 25, 50, 75 and 100% GA content, we use the c (2×2)×2 structure that was previously mentioned. We dope the aforementioned structure with the needed GA, make a number of initial guesses and then fully (vc-relax) the structures with no constraints. For 12.5% concentration, we use a 2×2×2 supercell. The relative internal energies reported in Fig. 1d are relative to the precursors, and the 0 has been chosen to be that of $FAPbBr_3$. The precursors are DFT-derived $PbBr_2$, GABr and FABr. The free energy is derived by adding the configurational entropy and (zero-temperature DFT-derived) internal energy contributions. The configurational entropy (per f.u.c. for $FA_{1-x}GA_xPbBr_3$) is calculated using the analytic formula for ideal alloys, which has been shown to be an effective model for entropy stabilization of hybrid perovskite systems: $S=k_B[x\ln x+(1-x)\ln(1-x)]$[36].

DFT calculations of acid or amine binding energies. An important part of our experiments is the stabilizing role of the long-chain acids and amines we synthesize our PNCs in. Specifically, we use oleic acid and decylamine. In order to understand how such ligands bind to our PNC's surfaces and how and what extent they stabilize these surfaces, we have performed DFT calculations. Using the picture above which points in the direction of AX-terminated surfaces, we study the interaction of acids and bases to such surfaces, and we investigate how the presence of surface GA groups changes the binding.

In order to understand the interaction between the ligands and the surface we performed a set of numerical experiments. We study the binding energy of the acid and amines as a function of their chain length (Supplementary Fig. 9). The surface binding energy of the ligand is sizable and is in the root of their stabilizing effect on our PNCs. The amines interact via their N-2p lone-pair with the proton-like nitrogen-bound hydrogen with the surface organic cation, while an amine hydrogen forms a hydrogen bond with the surface Br (Fig. 2b). The acid

interacts from the O end with the proton-like nitrogen-bound hydrogen of the surface organic cation; while the acid OH group interacts via its H with the surface Br (Fig. 2b). It can be seen that the interaction between the acids and amines can be decomposed into two parts: a) a strong point interaction that is present for smaller-chain acids and amines, b) a weaker non-local vdW interaction (Fig. 2c) that is a function of the chain length, the folding of the chain relative to the surface and to the neighboring ligands. The non-local part of the interaction closely depends on the specific orientation and folding of the ligand relative to the surface and neighboring ligands, which is naturally affected by the thermal motions and steric hindrance. Nevertheless, the property we are more interested in is the change in the ligand binding upon GA doping. Such a quantity is more robust and less dependent on the non-local part of the interaction, as the change in surface cation (FA to GA) mostly changes the local part of the interaction. Consequently, we quantify the change in the binding energy by introducing the GA via investigating the binding of short-chain acids and amines (acetic acid and ethylamine) which are dominated by the local point interactions (Supplementary Fig. 9a). To probe the trends in adsorption energies of some adsorbates using smaller adsorbates with identical chemical groups interacting with the surface is similar in philosophy to the idea of scaling relations in surface chemistry and catalysis. As mentioned in the main text, the GA doping slightly weakens the binding of these ligands (Supplementary Fig. 9b,c); this result is yet another indication that incorporating GA stabilizes the surface internally and decreases its reactivity toward external agents.

As a side note, the data used for Supplementary Fig. 9a to decompose the interaction of acids and amines as well as Fig 2b and 2c, have been generated based on an earlier set of calculations performed with a slightly higher energy bulk structure with an effective 1×1×1 reconstruction for $FAPbBr_3$, as opposed to c(2×2)×2. Nevertheless, the conclusions of these

figures are robust, as we extract the trends among binding energies and the nature of chemical bonds, as opposed to absolute value of binding energies. Even the absolute values vary insignificantly when compared to the numbers that correspond to the ground-state c(2×2)×2 reconstruction of the bulk $FAPbBr_3$. For example, the binding energies for acetic acid and ethylamine change by 0.02 eV, which do not change the conclusions made here for Supplementary Fig. 9a on the trend of binding energies.

Perovskite phase instability of $GAPbBr_3$. As mentioned in the main text, in the context of Fig. 1d, the perovskite phase of $GAPbBr_3$ (with D connectivity and corner sharing structure) is destabilized due to the large size of GA which is beyond the tolerance of the perovskite structure. The phase transition of $GAPbI_3$ to an edge-sharing phase has been experimentally observed and theoretically verified in a recent work. Both our DFT and experimental results also confirm that the perovskite structure is not a relevant phase for guanidinium lead bromide. Our DFT results show that a 1-dimensional (1D) edge sharing phase (e-phase) for $GAPbBr_3$ (Supplementary Fig. 11c), is enthalpically favored over the 3D perovskite phase by -0.11 eV per formula unit cell (f.u.c.). Additionally, as shown in Supplementary Fig. 4, the edge-sharing structure is even softer than the perovskite, thus is more entropically favored. Consequently, the 1D edge-sharing structure should possess a lower free energy than the 3D perovskite structure. DFT calculations show that the face-sharing phase (f-phase) does not have the enthalpy drive and is almost equal in internal energy to the perovskite phase. Moreover, one should note that our experimentally synthesized guanidinium lead bromide PNCs do not have to be in $GAPbBr_3$ stoichiometry. Another possibly relevant phase (as shown for the case of iodoplumbates) can be the GA-rich corner sharing 2D GA_2PbBr_4 structure (Supplementary Fig. 11b). Our experimental XRD patterns also confirm the deviation of the guanidinium lead bromide PNCs (x=1) from the perovskite structure (Supplementary Fig. 11d). Although we

have not been able to theoretically match the exact phase of guanidinium lead bromide (Supplementary Fig. 11e), it is clear that unlike lower values of *x* the structure is no longer in the corner-sharing perovskite phase.

Optical simulation of PeLEDs. In analyzing PeLEDs, the normalized power spectral densities were calculated using custom MATLAB codes based on the classical oscillating dipole approach. In order to separate outcoupling effect, internal quantum efficiency (IQE) is set to be unity. Since absorption loss of the emission layer (EML) is negligible in the emission spectra, lossless EML is assumed in the simulation for numerical stability. The refractive indices of Al, TPBi, EML(=$FA_{0.9}GA_{0.1}PbBr_3$), Buf-HIL, ITO, and glass used in the simulation were measured using spectroscopic ellipsometry (Woollam M2000D). For the refractive indices of TBTB layer, the refractive index of TPBI is applied because of its thin thickness (≈5nm). The emission zone was set to be located at the center of EML, which was supported by the electron/hole only device experiments.

Data Availability

The data that support the plots within this paper and other findings of this study are available from the corresponding author upon reasonable request.

References

43. Giannozzi, P. *et al.* QUANTUM ESPRESSO: A modular and open-source software project for quantum simulations of materials. *J. Phys. Condens. Matter* **21**, 395502 (2009).

44. Garrity, K. F., Bennett, J. W., Rabe, K. M. & Vanderbilt, D. Pseudopotentials for high-

throughput DFT calculations. *Comput. Mater. Sci.* **81**, 446–452 (2014).

45. Perdew, J. P., Burke, K. & Ernzerhof, M. Generalized gradient approximation made simple. *Phys. Rev. Lett.* **77**, 3865–3868 (1996).

46. Grimme, S., Antony, J., Ehrlich, S. & Krieg, H. A consistent and accurate ab initio parametrization of density functional dispersion correction (DFT-D) for the 94 elements H-Pu. *J. Chem. Phys.* **132**, 154104 (2010).

47. Wang, Y. *et al*. Density functional theory analysis of structural and electronic properties of orthorhombic perovskite $CH_3NH_3PbI_3$. *Phys. Chem. Chem. Phys.* **16**, 1424–1429 (2014).

48. Marzari, N., Vanderbilt, D., De Vita, A. & Payne, M. C. Thermal contraction and disordering of the Al(110) surface. *Phys. Rev. Lett.* **82**, 3296–3299 (1999).

49. Macrae, C. F. *et al.* Mercury CSD 2.0 - New features for the visualization and investigation of crystal structures. *J. Appl. Cryst.* **41**, 466–470 (2008).

50. Zhao, X.-G., Dalpian, G. M., Wang, Z. & Zunger, A. Polymorphous nature of cubic halide perovskites. *Phys. Rev. B* **101**, 155137 (2020).

Acknowledgements

This work was supported by the National Research Foundation of Korea (NRF) grant funded by the Korea government (MSIT) (NRF-2016R1A3B1908431). A.K., R.B.W., and A.M.R. acknowledge the support of the US Department of Energy, Office of Basic Energy Sciences, under grant DE-SC0019281 and also the computational support from NERSC of the DOE. P.T. acknowledges the scholarship from Chinese Scholarship Council (CSC). H.J.B. acknowledges funding from the European Research Council (ERC) under the European Union's Horizon 2020 research and innovation program (Grant agreement No. 834431) and the Spanish Ministry of Economy and Competitiveness (MINECO) via the Unidad de Excelencia María de Maeztu

MDM-2015-0538 and MAT2017-88821-R. A.S., S.N. and R.H.F. acknowledge support from the UKRI Global Challenge Research Fund project, SUNRISE (EP/P032591/1), UKIERI projects. S.N. acknowledges funding and support from Royal Society Newton-Bhabha international fellowship.

Author contributions

Y.-H.K, S. K. and A.K. equally contributed to this work. Y.-H.K, S. K. and T.-W. L. initiated and designed the study. Y.-H. K and S.K performed experiments and analyzed data. A.K., R.B.W. and P.T. performed the simulations, analyzed data, helped understand the structures and mechanisms behind the great efficiency. J.P., D.-H.K. and S.-H.J. helped to analyze the data. H.X. and B.-H. performed and analyzed magnetic field-dependent characteristics. Y.-H.L. and Y.-W.K. measured and analyzed TEM. L.M.-S. and H.J.B. commented on the synthesis of nanocrystals. J.-H. P. and S. Y performed optical simulation of the devices. A.S., S.N. and R.H.F. performed the PLQE measurements and analysis. A.M.R. and T.-W.L. supervised the study. All authors discussed the results and commented on the manuscript.

Competing interests

The authors declare no competing interests.

Additional information

Supplementary information is available for this paper

Reprints and permissions information is available at http://www.nature.com/

reprints.

Correspondence and requests for materials should be addressed to A.M.R. and T.-W.L

Comprehensive defect suppression in perovskite nanocrystals for high-efficiency light-emitting diodes

Young-Hoon Kim[1,2†], Sungjin Kim[1,2†], Arvin Kakekhani[3†], Jinwoo Park[1,2], Jaehyeok Park[4], Sung Heo[5], Yong-Hee Lee[1], Hengxing Xu[6], Satyawan Nagane[7], Dongwook Lee[5], Robert B. Wexler[3], Dong-Hyeok Kim[1,2], Seung Hyeon Jo[1,2], Laura Martínez-Sa--rti[8], Peng Tan[3,9], Aditya Sadhanala[7,10], Gyeong-Su Park[1], Young-Woon Kim[1], Bin-Hu[6], Henk J. Bolink[8], Seunghyup Yoo[4], Richard H. Friend[7], Andrew M. Rappe[3*], and Tae-Woo Lee[1,2*]

[1]Department of Materials Science and Engineering, Seoul National University, 1 Gwanak-ro, Gwanak-gu, Seoul 08826, Republic of Korea

[2]School of Chemical and Biological Engineering, Institute of Engineering Research, Research Institute of Advanced Materials, Nano Systems Institute (NSI), Seoul National University, 1 Gwanak-ro, Gwanak-gu, Seoul 08826, Republic of Korea

[3]Department of Chemistry, University of Pennsylvania, Philadelphia, Pennsylvania 19104, USA

[4]School of Electrical Engineering, Korea Advanced Institute of Science and Technology (KAIST), Daejeon 34141, Republic of Korea.

[5]Group for Molecular Engineering of Functional Materials, Ecole Polytechnique Fédérale de Lausanne, CH-1951 Sion, Switzerland

[6]Department of Materials Science and Engineering, University of Tennessee, Knoxville, TN 37996, USA

[7]Cavendish Laboratory, University of Cambridge, JJ Thomson Avenue, Cambridge CB3 0HE, U.K.

[8]Instituto de Ciencia Molecular (ICMol), Universidad de Valencia, Catedrático José Beltrán, 2, 46980 Paterna, Spain

[9]Department of Physics, Harbin Institute of Technology, Harbin 150001, China

[10]Clarendon Laboratory, Department of Physics, University of Oxford, Parks Road, Oxford OX1 3PU, UK.

[†] *These authors contributed equally to this work.*

**Authors to whom correspondence should be addressed: E-mail: twlees@snu.ac.kr, taewlees@gmail.com, rappe@sas.upenn.edu,*

Supplementary Discussion 1: DFT calculations of elastic properties.

Here, we computed the bulk elastic modulus using the stress-strain methodology[1–3]. In the Voigt-notation description, the relationship between the stress tensor σ_{ij} and strain tensor ε_{ij} within linear elasticity can be written as in equation (S1), where the C_{ij} are the elastic coefficients[4].

$$\begin{bmatrix} \sigma_1 \\ \sigma_2 \\ \sigma_3 \\ \sigma_4 \\ \sigma_5 \\ \sigma_6 \end{bmatrix} = \begin{bmatrix} C_{11} & C_{12} & C_{13} & C_{14} & C_{15} & C_{16} \\ C_{12} & C_{22} & C_{23} & C_{24} & C_{25} & C_{26} \\ C_{13} & C_{23} & C_{33} & C_{34} & C_{35} & C_{36} \\ C_{14} & C_{24} & C_{34} & C_{44} & C_{45} & C_{46} \\ C_{15} & C_{25} & C_{35} & C_{45} & C_{55} & C_{56} \\ C_{16} & C_{26} & C_{36} & C_{46} & C_{56} & C_{66} \end{bmatrix} \begin{bmatrix} \varepsilon_1 \\ \varepsilon_2 \\ \varepsilon_3 \\ \varepsilon_4 \\ \varepsilon_5 \\ \varepsilon_6 \end{bmatrix} \quad \text{(S1)}$$

For estimating the bulk moduli of GA-doped $FAPbBr_3$ structures, we first calculated all the 21 independent elastic coefficients in equation (S1). For calculations of the 21 independent elastic coefficients, a set of distorted structures are generated starting from a relaxed structure for each compound. Each structure in this set is deformed by one of the 6 independent elements in the strain tensor. We choose eight values for the strain magnitude, varying between −1 to +1%. That is, 48 deformed structures are calculated for each compound. For each of the imposed strains, the full stress tensor is obtained from a DFT calculation in which ionic relaxations are included. Further, using the linear stress-strain relationship in equation (S1), all elastic coefficients are derived from the corresponding linear fits of the calculated stresses over the range of the applied strains, respectively. When the absolute value of the fitting result of an elastic coefficient is less than 0.20 Gpa, we assumed that the value of this constant is approximately equal to zero, considering the deviation of linear fits of the calculated stresses. We provided all the 21 coefficients for these materials here, as shown in Supplementary Table 5. Using these coefficients, we calculated the Voigt and Reuss averages for the effective bulk moduli of these GA-doped $FAPbBr_3$ structures. The Voigt and Reuss averages are the upper

and lower bounds for elastic moduli, respectively. The 9 coefficients in Supplementary Table 5a are dominant in both Voigt and Reuss averages. The 12 coefficients in Supplementary Table 5b only affect Reuss average through compliance constants S_{ij}, where the S_{ij} tensor is the inverse of C_{ij} tensor. The Voigt and Reuss effective bulk moduli are as follows:

$$B_{\mathrm{V}} = \frac{1}{9}\left[(C_{11} + C_{22} + C_{33}) + 2(C_{23} + C_{13} + C_{12})\right] \tag{S2}$$

$$B_{\mathrm{R}} = \frac{1}{\left[(S_{11} + S_{22} + S_{33}) + 2(S_{23} + S_{13} + S_{12})\right]} \tag{S3}$$

where B represents bulk modulus, and subscripts V and R correspond to the Voigt average and the Reuss average, respectively[3,5,6]. Also, the Voigt-Reuss-Hill average, which is the average of the Voigt and the Reuss elastic moduli, is also provided. This empirical average is known to represent the elastic modulus with extremely high accuracy. The bulk modulus from the Voigt-Reuss-Hill average is calculated by

$$B_{\mathrm{VRH}} = \frac{B_{\mathrm{V}} + B_{\mathrm{R}}}{2} \tag{S4}$$

where the subscript VRH represents the Voigt-Reuss-Hill average.

We calculated the elastic properties of $FAPbBr_3$, $(FA)_{0.875}(GA)_{0.125}PbBr_3$, $(FA)_{0.75}(GA)_{0.25}PbBr_3$, $(FA)_{0.50}(GA)_{0.50}PbBr_3$, $(FA)_{0.25}(GA)_{0.75}PbBr_3$, and $GAPbBr_3$, respectively. The elastic coefficients C_{ij} for the 5 compounds are shown in Supplementary Table 5. All the C_{ij} matrices of these materials satisfy the generic necessary and sufficient elastic stability condition that all eigenvalues of the C_{ij} matrix are positive[7]. By the equations (S2-S4), the corresponding effective bulk moduli are calculated as in Supplementary Table 6. The errors in B_V are estimated from the standard errors in the linear fits of C_{11} to C_{66}, and the so-estimated mean error in bulk moduli is nearly 0.23 GPa. The bulk modulus, varying with the GA-doped ratio x, is shown in Supplementary Fig. 4: as it can be seen past *x*=0.25 the structure abruptly

softens, which is a result of perovskite structure destabilization which basically leads to an effective loss of connectivity.

In Supplementary Fig. 11, and for x=1 (only GA) we considered three possible structures, that is, FA_0GA_1 (corner-sharing perovskite), GA_2PbBr_4 (corner-sharing), and $GA_{e\text{-}phase}$ (edge-sharing). Because the types of connectivity in FA_0GA_1, GA_2PbBr_4, and $GA_{e\text{-}phase}$ are 3D, 2D and 1D, respectively, there are the highest degrees of freedom in $GA_{e\text{-}phase}$ structure (Supplementary Fig. 11c). Hence, $GA_{e\text{-}phase}$ has the smallest bulk modulus, while FA_0GA_1 has the largest bulk modulus in the three possible structures. Here, FA_0GA_1 refers to the perovskite phase (corner sharing with 3D connectivity) of $GAPbBr_3$ while $GA_{e\text{-}phase}$ refers to the edge-sharing $GAPbBr_3$ structures with 1D connectivity.

Supplementary Discussion 2: DFT calculations of surfaces.

Our surface calculations are based on an in-plane periodicity of c(2×2). For example, to model the $FAPbBr_3$(001) surface, we take the fully-vc-relaxed c(2×2)×2 bulk structure of $FAPbBr_3$, make several copies in the *z*-direction, and terminate the structure in this direction by introducing a vacuum of ≈15 Å. Such a slab contains five layers of $PbBr_2$ and five layers of FABr, where the atoms in the bottom five layers are fixed to their bulk positions to simulate the proper mechanical boundary conditions on the top (free to relax) layers. We then relax the atomic coordinates of the top layers of the slab.

The first step toward modeling PeLED properties on perovskite nanocrystal surfaces was answering the basic question "how do these surfaces terminate?" To this purpose, we made surface phase diagrams to determine the most stable surface phase. Surface phase diagrams for (Mol)$PbBr_3$, where Mol∈{FA,GA} are constructed using *ab-initio* thermodynamics [8]. We start by defining the conditions under which (Mol)$PbBr_3$ is stable, *i.e.* when:

$$\mu_{Mol}+\mu_{Pb}+3\mu_{Br}=G\ ((Mol)PbBr_3(s)) \tag{S5}$$

where μ is the chemical potential and *G* is the Gibbs free energy. It is convenient to calculate μ relative to some reference state, *e.g.*,

$$\Delta\mu_{Mol} = \mu_{Mol} - E^{DFT}_{Mol(g)} \tag{S6a}$$

$$\Delta\mu_{Pb} = \mu_{Pb} - E^{DFT}_{Pb(s)} \tag{S6b}$$

$$\Delta\mu_{Br} = \mu_{Br} - E^{DFT}_{Br(s)} \tag{S6c}$$

where E^{DFT} is the DFT total energy per formula unit and Pb(*s*) is face-centered cubic ($Fm\bar{3}m$ space group [225]). While Br is a liquid at ambient temperatures, DFT

calculations correspond to 0 K. Therefore, we use the ground-state crystal structure of Br at 0 K (orthorhombic, Cmce space group [64]) as the reference state for μ_{Br}. Inserting equations S6a, S6b, and S6c into equation S5 yields

$$\Delta\mu_{Mol}+\Delta\mu_{Pb}+3\Delta\mu_{Br}=\Delta G_f\,((Mol)PbBr_3(s)) \quad \text{(S7)}$$

where ΔG_f is the Gibbs free energy of formation.

(Mol)$PbBr_3$ can decompose into Pb(*s*), Br(*s*), (Mol)Br(*s*), and PbBr(*s*) thus giving rise to the following four stability criteria:

$$\Delta\mu_{Pb} < 0 \quad \text{(S8a)}$$

$$\Delta\mu_{Br} < 0 \quad \text{(S8b)}$$

$$\Delta G_{f,(Mol)PbBr_3(s)} - \Delta\mu_{Pb} - 2\Delta\mu_{Br} < \Delta G_{f,(Mol)Br(s)} \quad \text{(S8c)}$$

$$\Delta\mu_{Pb} + \Delta\mu_{Br} < \Delta G_{f,PbBr_2(s)} \quad \text{(S8d)}$$

These criteria do not depend on $\Delta\mu_{Mol}$ because it is defined by $\Delta\mu_{Pb}$ and $\Delta\mu_{Br}$ via equation S7. For Mol∈{MA,FA,GA}, we find that decomposition into (Mol)Br and $PbBr_2$ is spontaneous for all $\Delta\mu_{Pb}$ and $\Delta\mu_{Br}$. Previous theoretical studies report a narrow bulk stability region (BSR) for $MAPbBr_3$ due to the small thermodynamic barrier for its decomposition into MABr and PbBr (0.19 eV)[9,10]. A narrow BSR has also been reported for $MAPbI_3$[11–13]. It has been suggested that the relative instability of $FAPbBr_3$ can be attributed to (1) the shallower and more asymmetric electrostatic potential surrounding Br, (2) the larger size of FA, which elongates and therefore weakens Pb-Br bonds in the inorganic sublattice, and (3) the smaller dipole on FA, which decreases the dipolar contribution to the electrostatic energy[14]. Since GA is larger and less polar than FA, arguments (2) and (3) can also be used to explain why perovskite $GAPbBr_3$ (with 3D connectivity) is unstable.

Despite our computational prediction that $MAPbBr_3$ and $FAPbBr_3$ are enthalpically

unstable, we have synthesized perovskite nano-crystals (PNCs) out of them and have shown that they are resistant to decomposition. One possible reason for this apparent discrepancy is the absence of entropic contributions to *G*, arising from vibrations and molecular rotations, in our computational treatment. Also, the PNCs have significant surface stabilization from ligands. The less stable a material becomes, *e.g.* upon replacing MA with FA or GA in (Mol)PbBr, the softer its vibrations become thus increasing the entropy contribution to the stability at ambient temperatures due to vibrational entropy. Including these entropic contributions, however, is beyond the capabilities of highly optimized DFT codes even on the most sophisticated and powerful computational architectures. With that being said, the placement of the $PbBr_2$ boundary (black line in Supplementary Fig. 1a-c) should be less affected by entropy than (Mol)$PbBr_3$ because it has harder vibrations and lacks constituents with rotational degrees of freedom. Therefore, we will assume that there is an infinitesimally narrow BSR starting from this line and moving up and to the right in the surface phase diagrams (Supplementary Fig. 1a-c).

In our surface stability analysis, we consider four (001) terminations of FAPbBr: _$PbBr_2$, _$PbBr_2$+vac, _FABr, and _FABr+vac (Supplementary Fig. 1d-f). Their surface energies (γ) are calculated for various conditions using the following expression:

$$\gamma = \frac{1}{2A}(\gamma^0 + \Delta\gamma) \tag{S9}$$

where *A* is the area of the surface unit cell and

$$\gamma^0 = \frac{1}{2A}\left(E^{DFT}_{slab} - N_{Mol}\Delta G_{f,(Mol)PbBr_3(s)} + \Gamma_{Pb}E^{DFT}_{Pb(s)} + \Gamma_{Br}E^{DFT}_{Br(s)}\right) \tag{S10a}$$

$$\Delta\gamma = \frac{1}{2A}(\Gamma_{Pb}\Delta\mu_{Pb} + \Gamma_{Br}\Delta\mu_{Br}) \tag{S10b}$$

$$\Gamma_{Pb} = N_{Mol} - N_{Pb} \tag{S10c}$$

$$\Gamma_{Br} = 3N_{Mol} - N_{Br} \tag{S10d}$$

Here, $E_{\mathrm{slab}}^{\mathrm{DFT}}$ is the DFT total energy of the slab and N_X is the number of species X in the slab. Supplementary Fig. 1a shows the surface phase diagram of $FAPbBr_3$(001) constructed using equations S9 and S10. Only two surface phases are observed in the window of $\Delta\mu_{Pb}$ and $\Delta\mu_{Br}$ and containing the BSR of $FAPbBr_3$: _$PbBr_2$ and _FABr. The most stable surface phase is that which is present in the BSR of $FAPbBr_3$, *i.e.* at the $PbBr_2$ boundary (black line in Supplementary Fig. 1a-c. As such, we predict that the _FABr surface is exposed in our experiments, which is in agreement with previous theoretical and experimental research on $MAPbX_3$ where X∈{I,Br,Cl}[9,11–13,15–18]. In the presence of ligands (Supplementary Fig. 1b,c), _$PbBr_2$ is stabilized relative to _FABr. This is due to the deeper electrostatic well created by the Pb^{2+} cation, as opposed to FA^+, which creates a stronger electrostatic bond with the lone pair of the acid's O or amine's N [19]. In Supplementary Fig. 1a-c, we have identified cases with absolute and less extreme upper bound for ligand stabilization. In the former, each site (FA^+ or Pb^{2+}, depending on the termination) is supposed to bind and get stabilized by the ligand; while for the latter, half the sites are supposed to have a bound ligand. Due to the steric hindrance of the long chain acids and amines we use in our experiments, the less extreme bound might be a more realistic choice. This stabilization, however, is not enough to shift the equilibrium between _$PbBr_2$ and _FABr such that _$PbBr_2$ is in the BSR of $FAPbBr_3$. Therefore, even upon ligand stabilization, _FABr is preferred. We also point out the equilibrium between _$PbBr_2$ and _$PbBr_2$+vac (white lines in Supplementary Fig. 1a-c) in response to recent theoretical work suggesting that _$PbBr_2$+vac is the most stable surface phase[13]. We find, however, that in the region of and where this equilibrium occurs, _FABr is the favored termination.

Equipped with the knowledge of which surface termination is thermodynamically favored, we construct our surface models of the $FAPbBr_3$-based PNCs. The first question we would like to answer is the critical concentration for GA, beyond which the GA is pushed to surface. For this purpose, we build a model of GA covered $FAPbBr_3$(001) surfaces (Fig. 2d). According to

our findings on formation free energies of $FA_{1-x}GA_xPbBr_3$ phase as a function of x (Fig. 1d), the GA can favorably dissolve in $FAPbBr_3$ in very low concentration regime (up to $x \approx 12.5\%$). So based on our bulk calculations, it seems that beyond this concentration the extra GA is pushed out of the perovskite structure (to the surface). Additionally, we calculate the energy of GA terminated surfaces (Fig. 2d), and compare the energetics of a) GA in the perovskite bulk (in low concentration x=12.5%) and FA terminating the surface with b) GA forming a surface terminating layer and FA being in the bulk. Based on our DFT calculations, we find that such a number is almost zero for x=12.5%; which means above 12.5%, in which the GA gets more enthalpically penalized in the bulk, the GA then favorably is pushed to the surface and has a thermodynamic drive to form a full GA terminated monolayer.

In addition to extended surfaces, we also build a (FA (A-cation) terminated) quantum dot (Qdot) model to more directly represent the $FAPbBr_3$-based PNCs (Fig. 3d). The full FA Qdot, has 567 atoms and the Qdot is located in a cubic simulation cell, each side $\approx$30 Å. Such a large cell size puts enough vacuum on each side between the periodic copies of the Qdot. The atomic coordinates in the Qdots are fully relaxed with convergence parameters previously mentioned. In order for our Qdots to have charge balance and charge neutral, we have to adjust the stoichiometry and remove 2 FAs on one of the edges. We have also built a $GAPbBr_3$ Qdot and a GA-shell FA-core Qdot model.

Another property we are interested to quantify is the extra resistance of GA-terminated surfaces towards defect generation. For this purpose, as mentioned in the main text, we calculate the cohesive energy of the surface, defined as the binding energy of the top GABr layer relative to the degradation products (Guanidine(g) and HBr(g))[20,21] and compare this value to that of FABr layer on FA-terminated surfaces (degradation to Formamidine(g) and HBr(g)). The extra amino group in GA (compared to FA) creates more hydrogen bonds with its neighboring Br groups and boost the surface adhesion. The extra stabilization quantified

using the aforementioned metric is -350 meV (per GA) for the extended surfaces (GABr terminated $FAPbBr_3$(001) slab) and -390 meV for Qdots with FA-core and GA-shell. The extra stabilization that is calculated for the Qdots is a result of the existence of more under-coordinated sites (e.g., corner and edges) in the Qdots. It should be noted that in order to find the stabilizing effect of GA in the Qdots, we shaved a GABr/FABr unit from the Qdots and re-relaxed the resulting Qdot; then the average effect of GA was determined by normalizing the binding energy of the top layer by the number of shaved GABr/FABr units (12 to be specific).

Another type of calculations we performed was on a surface with Br vacancy to understand the healing effect of TBTB. The Br vacancy was created on a c(2×2) GA-terminated $FAPbBr_3$ surface. We take out a surface Br atom and re-relax the supercell. Thus, the surface with Br vacancy is charge neutral and metallic (having one electron per Br in the conduction band). This can be also interpreted to correspond to a surface with Br^- vacancy (leading to an insulating system with a total positive charge) that can trap an electron (becoming charge neutral). The reaction energy for TBTB debromination (leading to a spin-polarized radical with 1 μ_B) and vacancy filling is -1.89 eV. The great absolute value of this number means that such a reaction cannot only be driven using trapped electrons with high energies (close to the material's conduction band), but also using electrons with lower energies (that fall deeper into the material's bandgap which is calculated to be 1.96 eV). In short, if such a system is pumped with electrons that are at least 0.1 eV more energetic than the valence band, there is a favorable thermodynamic drive for Br vacancies to be filled by the TBTB; this is certainly the case in an LED device setting or a photovoltaic system subject to light irradiation. After the vacancy healing and the TBTB debromination, the resulting radical can get hydrogenated with a reaction energy of -1.70 eV (relative to 0.5 H_2(g)). This is a great hydrogen affinity (to be compared with -2.25 eV per atom DFT-derived atomization energy of H_2(g)), and shows that the debrominated radical will favorably get further hydrogenated, probably by acquiring a

hydrogen from the acid ligands surrounding the PNC.

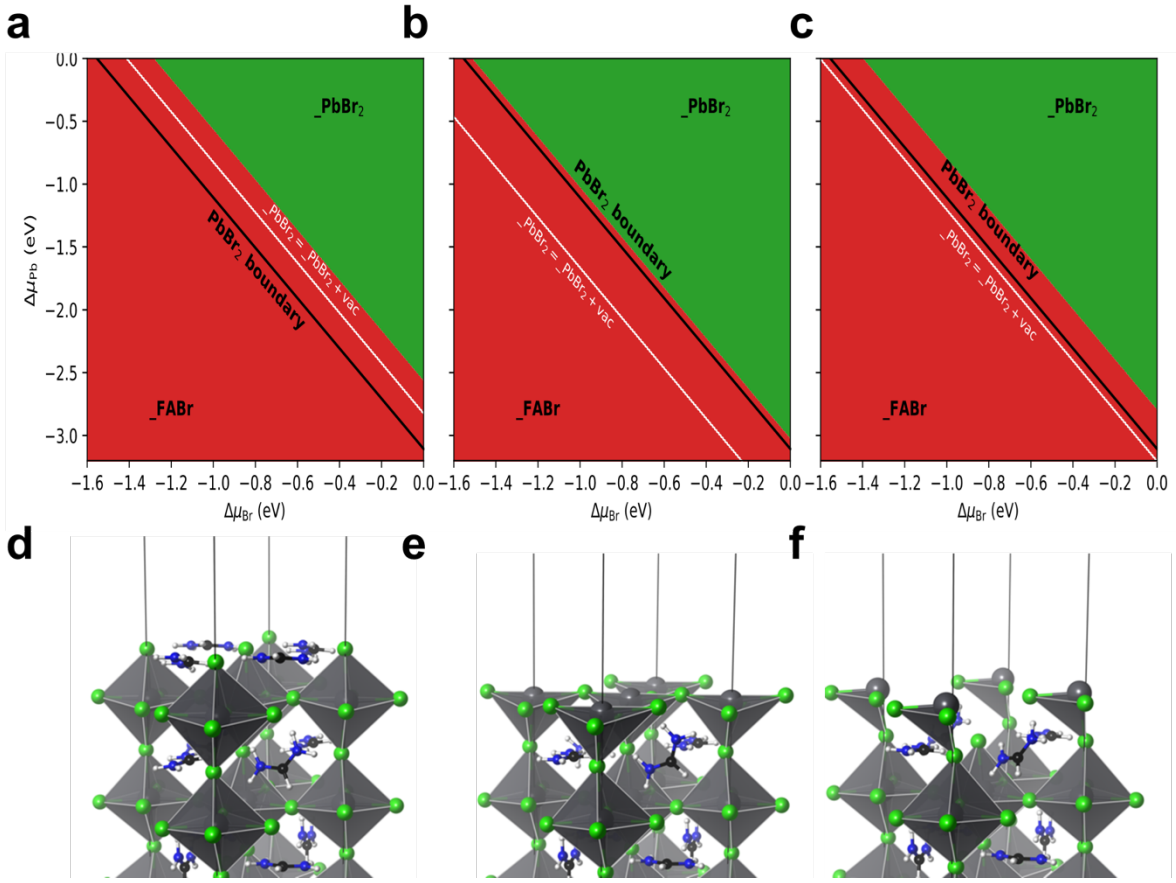

Supplementary Fig. 1 | Surface phase diagram for $FAPbBr_3$. a-c, (001) surface phase diagram of $FAPbBr_3$ without **(a)** and with absolute upper bound ligand stabilization **(b)**, and with less extreme upper bound ligand stabilization **(c)**. The black line corresponds to the $PbBr_2$ boundary of the bulk stability region (BSR) for $FAPbBr_3$. The white line corresponds to the equilibrium between $\_PbBr_2$ and $\_PbBr_2$+vac. **d-f,** FABr-terminated (**d**), $PbBr_2$-terminated (**f**) and $PbBr_2$ vacancy terminated (**f**) surface phases we simulate to create surface phase diagrams for $FAPbBr_3$(001) surfaces. For more details see Supplementary Discussion 2.

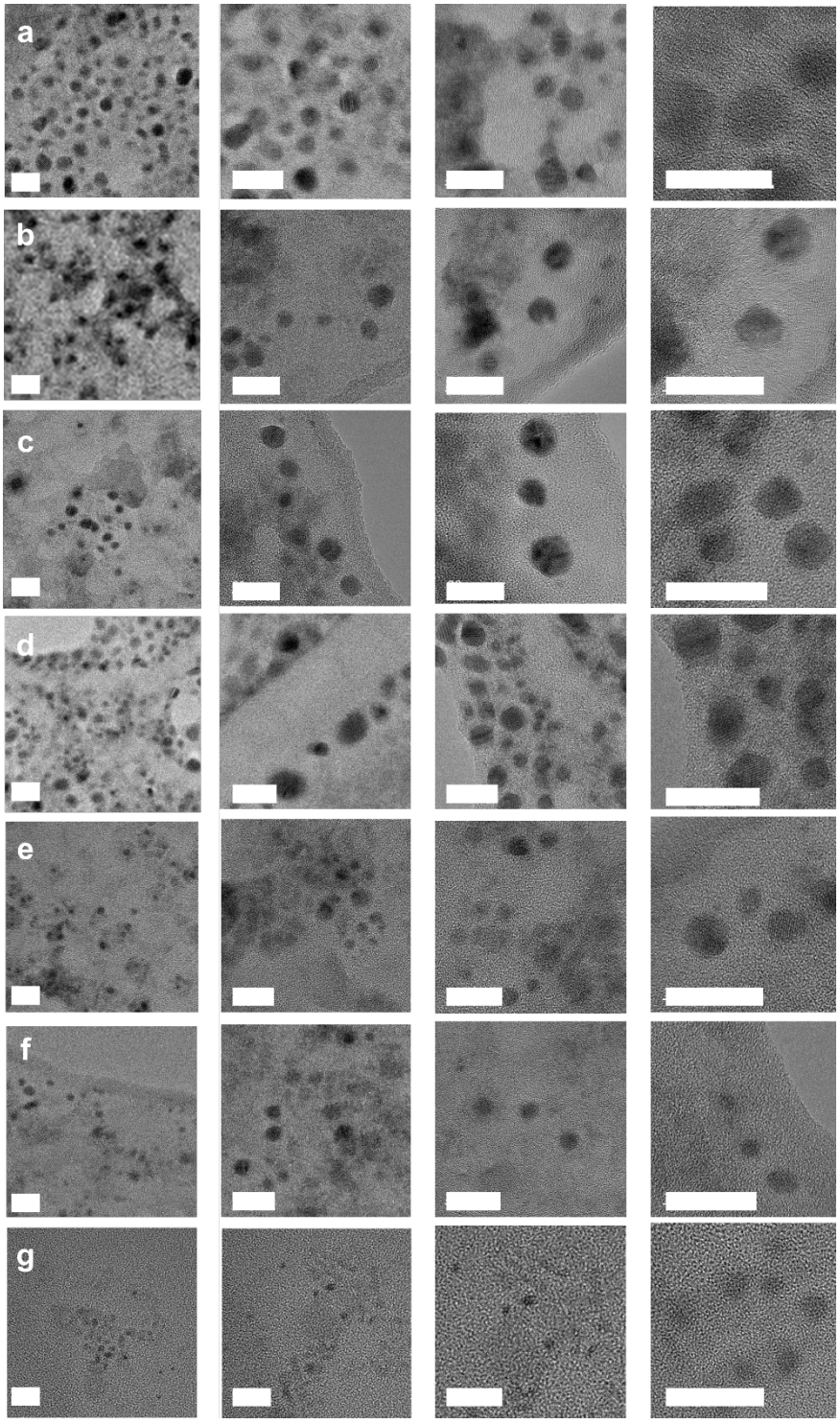

Supplementary Fig. 2 | Transmission electron microscopy (TEM) image of $FA_{1-x}GA_xPbBr_3$ PNCs with different *x*; a-g, $FAPbBr_3$ (**a**), $FA_{0.95}GA_{0.05}PbBr_3$ (**b**), $FA_{0.9}GA_{0.1}PbBr_3$ (**c**), $FA_{0.8}GA_{0.2}PbBr_3$ (**d**), $FA_{0.7}GA_{0.3}PbBr_3$ (**e**), $FA_{0.4}GA_{0.6}PbBr_3$ (**f**), and $FA_{0.2}GA_{0.8}PbBr_3$ (**g**) PNCs (scale bar: 20 nm).

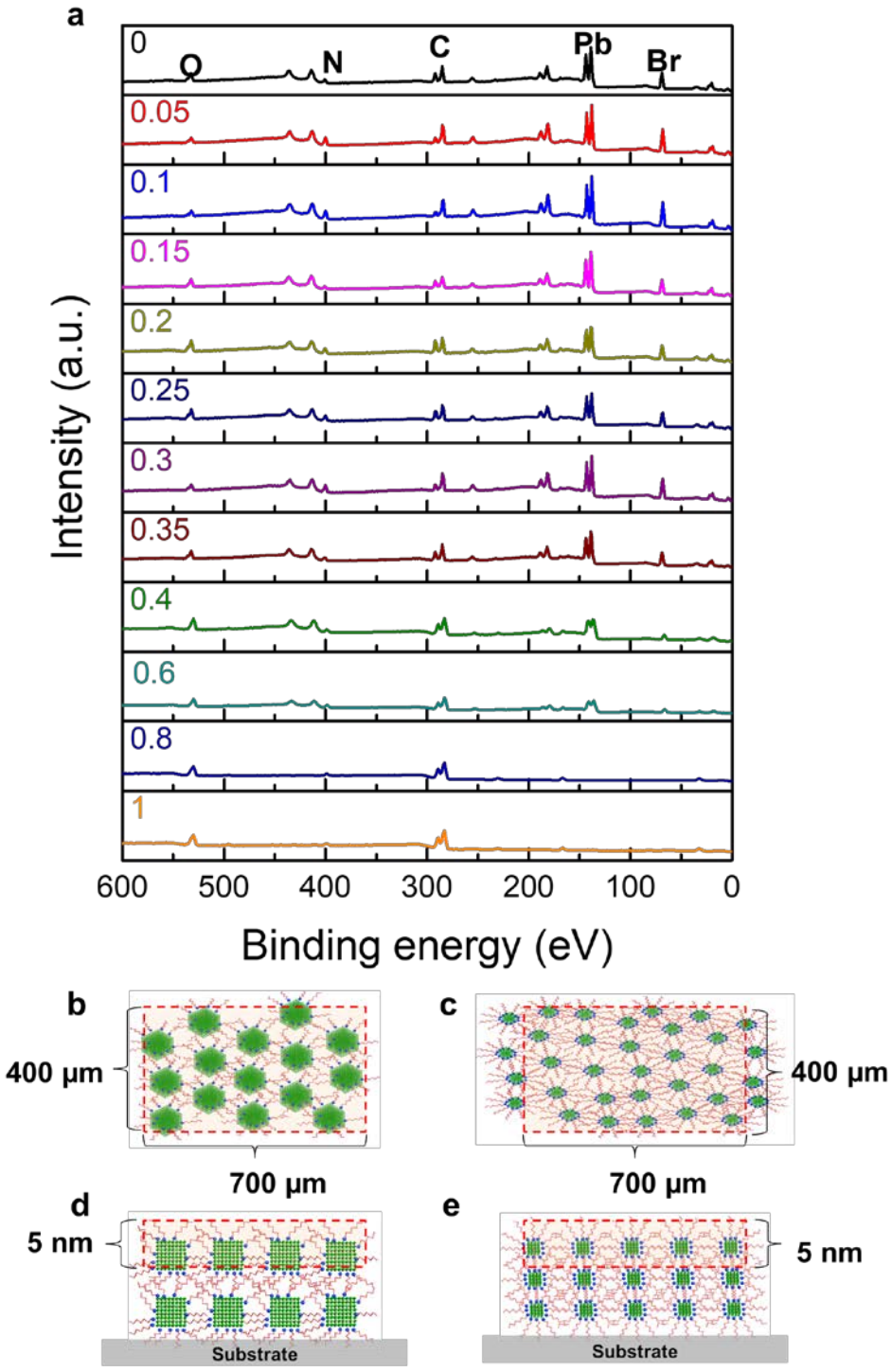

Supplementary Fig. 3 | X-ray photoelectron spectroscopy (XPS) analysis of $FA_{1-x}GA_xPbBr_3$ PNC films. **a,** XPS spectrum of $FA_{1-x}GA_xPbBr_3$ PNCs with different *x*. **b-e,** A schematic illustration of the XPS measurements for larger perovskite PNCs (top view) (**b**), smaller PNCs (top view) (**c**), larger PNCs (side view) (**d**), and smaller PNCs (side view) (**e**).

As *x* increases, $FA_{1-x}GA_xPbBr_3$ PNCs showed gradually decreasing intensities of Pb and Br peaks relative to the consistent intensities of the O peak (**Supplementary Fig. 3a**). Signals of Pb and Br are from $FA_{1-x}GA_xPbBr_3$ crystals and the O signal arises from organic ligands (oleic acid). These results indicate that as *x* increases, the size of $FA_{1-x}GA_xPbBr_3$ PNCs decreases and thus, the proportion of organic ligands compared to $FA_{1-x}GA_xPbBr_3$ crystals and surface-to-volume ratio of PNCs increase.

We think that the relative size change of perovskite NCs can be investigated by XPS due to the large measurement area of the XPS spectrometer (400 μm × 700 μm, AXIS Nova, KRITOS corporation). In the larger PNCs, the relatively small amount of the organic ligands can be detected compared to the inorganic backbone of the perovskite, while in smaller PNCs, a relatively large amount of organic ligands can be measured (**Supplementary Fig. 3b-e**). Note that the surface binding ligands scale as a function of surface area, while the inorganic signature scales as a function of volume; consequently, larger surface to bulk ratio means a relatively larger organic signature in the XPS. Indeed, measuring the peak intensity ratio of organic to inorganic elements can reflect the general trend of PNCs' relative size change (as per the **Supplementary Fig. 3a**).

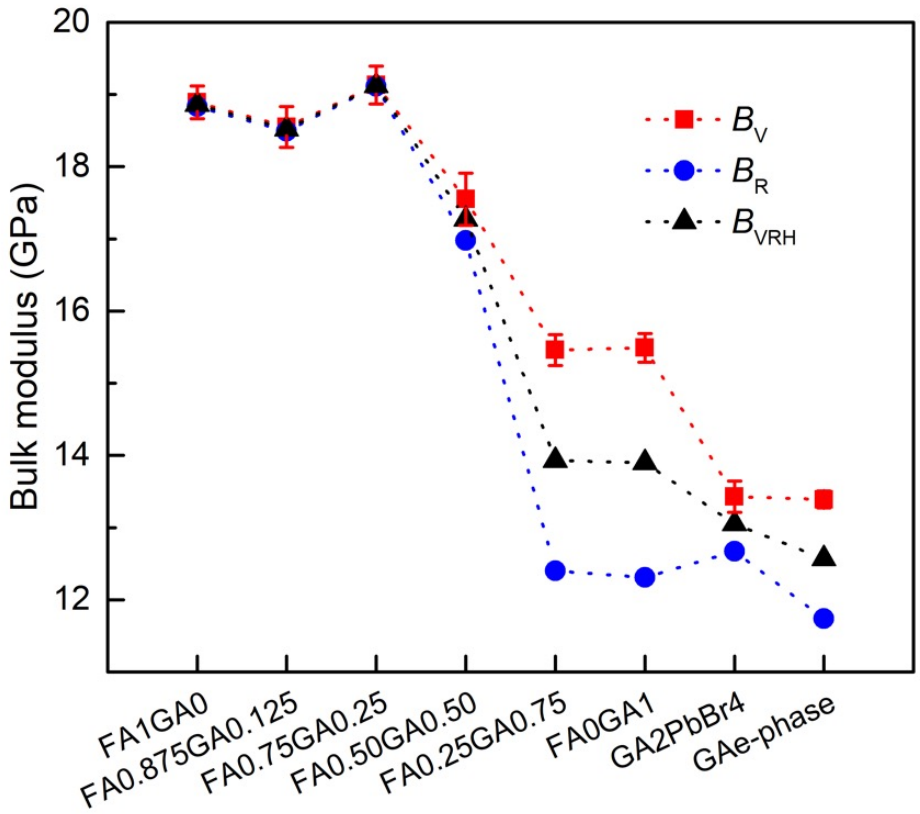

Supplementary Fig. 4 | Elastic bulk moduli of $FA_{1-x}GA_xPbBr_3$. Maximum bulk modulus in low concentration of GA indicate that beyond the low concentrations, GA cations have an energetic preference to migrate to the surface rather than be incorporated in crystal lattices. Here, FA_0GA_1 refers to the perovskite phase (corner sharing with 3D connectivity) of $GAPbBr_3$ while $GA_{e\text{-}phase}$ refers to the edge-sharing $GAPbBr_3$ structures with 1D connectivity. For more details see Supplementary Discussion 1.

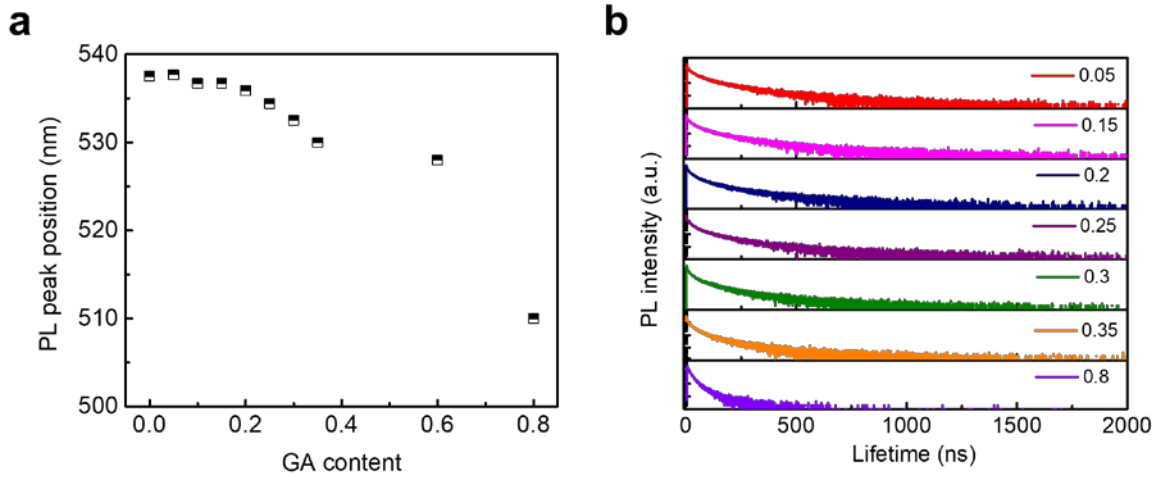

Supplementary Fig. 5 | PL peak position and transient PL of $FA_{1-x}GA_xPbBr_3$ PNCs. a, PL peak position of $FA_{1-x}GA_xPbBr_3$ PNCs with different *x*. **b**, PL lifetimes of $FA_{1-x}GA_xPbBr_3$ PNCs (*x* = 0.05, 0.15, 0.2, 0.25, 0.3, 0.35, 0.8).

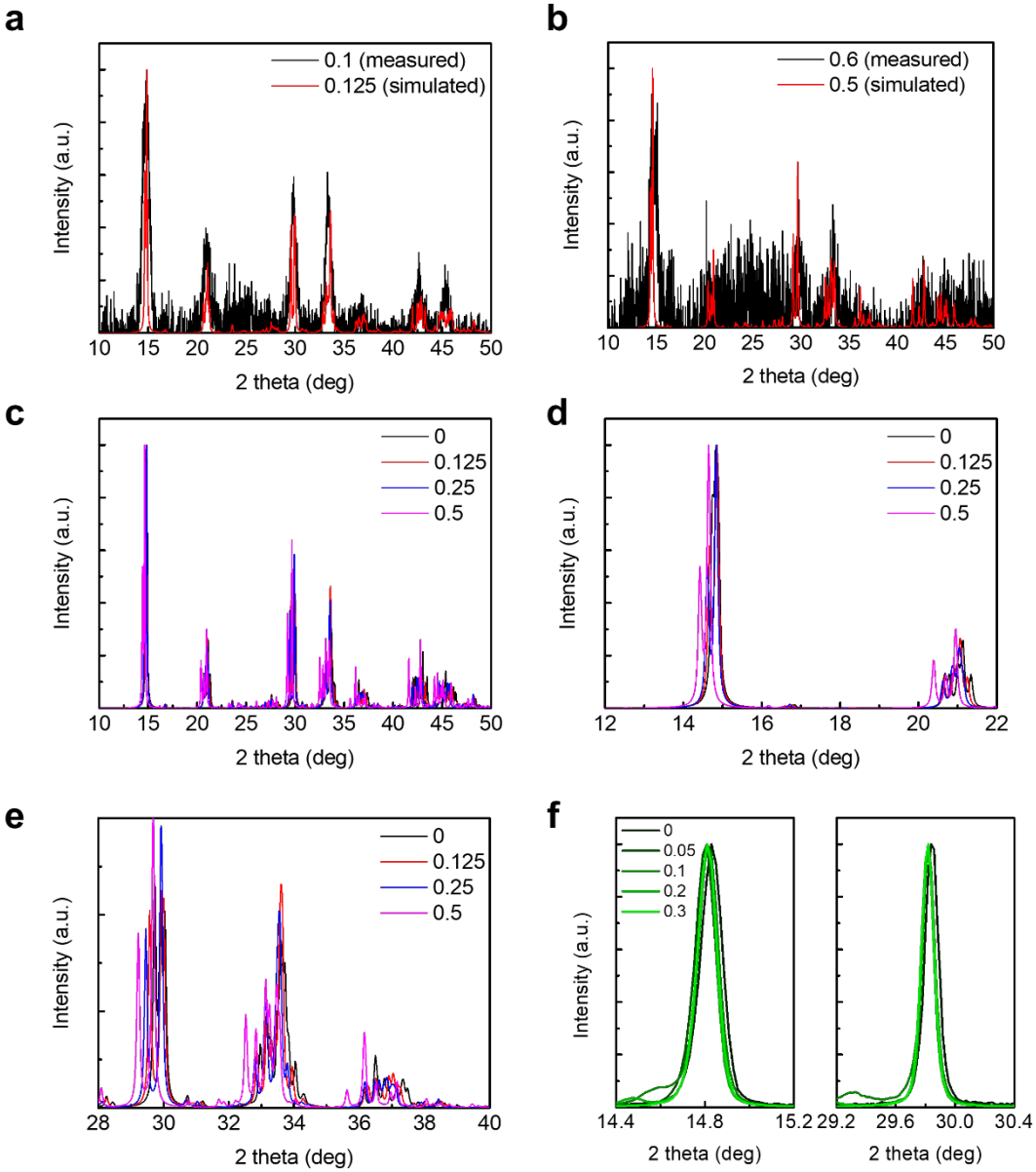

Supplementary Fig. 6 | X-ray diffraction (XRD) analysis of $FA_{1-x}GA_xPbBr_3$. a, Measured XRD patterns of $FA_{0.9}GA_{0.1}PbBr_3$ PNCs and simulated XRD patterns of $FA_{0.875}GA_{0.125}PbBr_3$. **b,** Measured XRD patterns of $FA_{0.4}GA_{0.6}PbBr_3$ PNCs and simulated XRD patterns of $FA_{0.5}GA_{0.5}PbBr_3$. **c-e,** Simulated XRD patterns of $FA_{1-x}GA_xPbBr_3$ with different *x* (0, 0.125, 0.25, 0.5) in the range of 10 to 50 deg (**c**), 12 to 22 deg (**d**) and 28 to 40 deg (**e**) by assuming that all GA cations are incorporated into $FA_{1-x}GA_xPbBr_3$ crystal structure. **f,** Measured XRD patterns regarding (100) plane (left) and (200) plane (right) of $FA_{1-x}GA_xPbBr_3$ polycrystalline bulk films with different *x*.

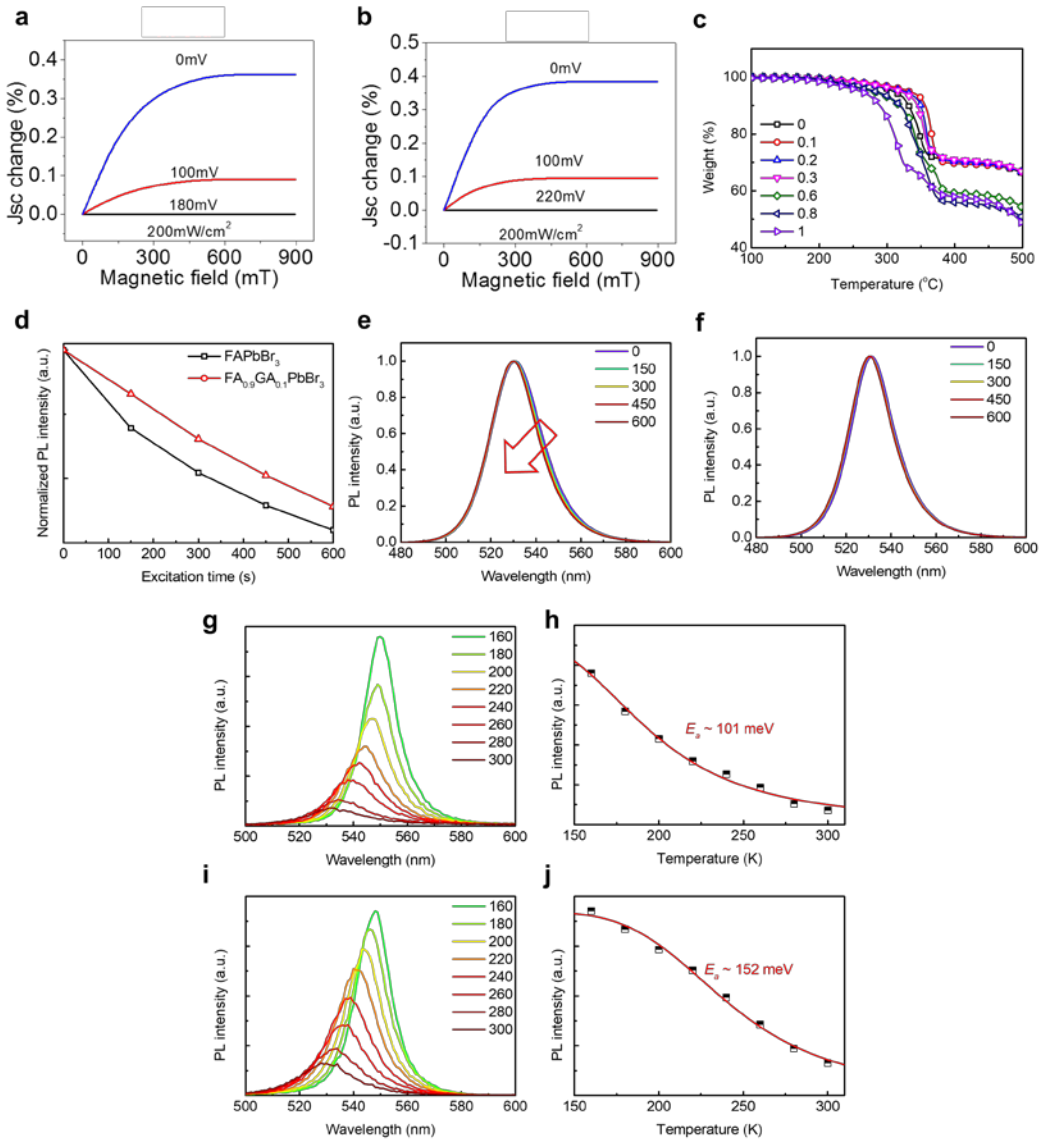

Supplementary Fig. 7 | Analysis of GA doping effects on the $FA_{1-x}GA_xPbBr_3$ PNCs. a, b, Magneto-photocurrent (MPC) of PeLEDs based on $FAPbBr_3$ (**a**) and $FA_{0.9}GA_{0.1}PbBr_3$ (**b**) PNCs under different reverse biases. **c,** Thermogravimetric analysis (TGA) representing weight loss curve of $FA_{1-x}GA_xPbBr_3$ PNCs with different *x*. **d,** Normalized PL intensities of $FAPbBr_3$ and $FA_{0.9}GA_{0.1}PbBr_3$ PNC films. **e, f,** Normalized PL spectrum of $FAPbBr_3$ (**e**) and $FA_{0.9}GA_{0.1}PbBr_3$ (**f**) PNC films under constant laser excitation (time scale: s). **g-j,** Temperature (*K*) dependent PL spectrum and maximum PL intensity with calculated activation energy of $FAPbBr_3$ PNCs (**g**), (**h**) and $FA_{0.9}GA_{0.1}PbBr_3$ PNCs (**i**), (**j**). Measurements were conducted in vacuum.

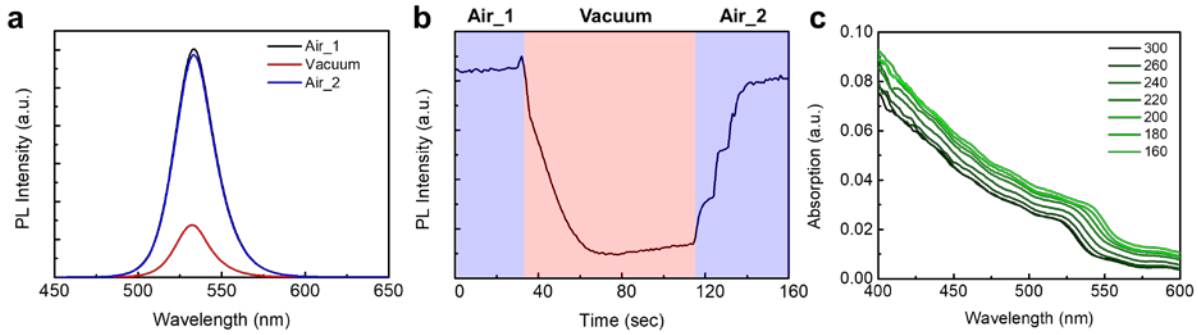

Supplementary Fig. 8 | Atmospheric condition dependent PL and temperature dependent absorption of $FA_{0.9}GA_{0.1}PbBr_3$ PNC films. a, PL spectrum of $FA_{0.9}GA_{0.1}PbBr_3$ PNC film in ambient air and in vacuum at room temperature. **b,** Dynamics of PL peak maximum of $FA_{0.9}GA_{0.1}PbBr_3$ PNC film under gradual evacuation and ventilation of atmospheric conditions. **c,** Temperature (*K*) dependent absorption spectrum of $FA_{0.9}GA_{0.1}PbBr_3$ PNC film in vacuum.

To study the increasing PL intensity with decreasing temperature in **Supplementary Fig. 7g-j**, we consider the atmospheric conditions of the samples when the PLQE and temperature dependent PL measurements were conducted; we measured the PLQE in air at room temperature, while the temperature dependent PL was measured in vacuum in a closed cycle cryostat (Advanced Research Systems, Inc.). To compare the effects of atmospheric conditions on PL intensity, we measured the PL intensity of $FA_{0.9}GA_{0.1}PbBr_3$ PNCs in air and in vacuum at room temperature (**Supplementary Fig. 8a,b**). $FA_{0.9}GA_{0.1}PbBr_3$ PNCs showed around 4.5 times improved PL intensity in air than in vacuum, which is reversible. We attribute the high PL intensity of PNCs in air to the partial passivation of defects by O_2 molecules[22,23]. Although the surface GA cations have a beneficial effect in suppressing surface defects, there can still be defects in the bulk of the material. O_2 molecules are small enough that can diffuse inside the PNC and help passivate the bulk defects, in addition to the surface defects. As shown in **Supplementary Fig. 7g-j**, the PL intensity increases manifold once decreasing the temperature down to 160 *K*. Although the PNCs show, for instance, around 25% increase in absorption at 405 nm with decreasing temperature down to 160 *K* (**Supplementary Fig. 8c**), this change in

absorption is not enough to be the main reason behind the manifold increase in PL intensity.

The temperature dependence measurements were performed on samples in vacuum. Unlike the case of PNCs in air, such samples do not benefit from O_2 defect passivation effects. DFT calculations have recently shown that the coupling between phonons and defects (*e.g.*, Br vacancy) can cause the defect energy levels to thermally fluctuate (by as large as 1 eV at room temperature)[24]. Such fluctuations can render a shallow transition level into a deeper one and increase non-radiative recombination. Hence, we hypothesize that the increasing PL intensity in lower temperatures can be attributed to a decreasing coupling between phonons and defects.

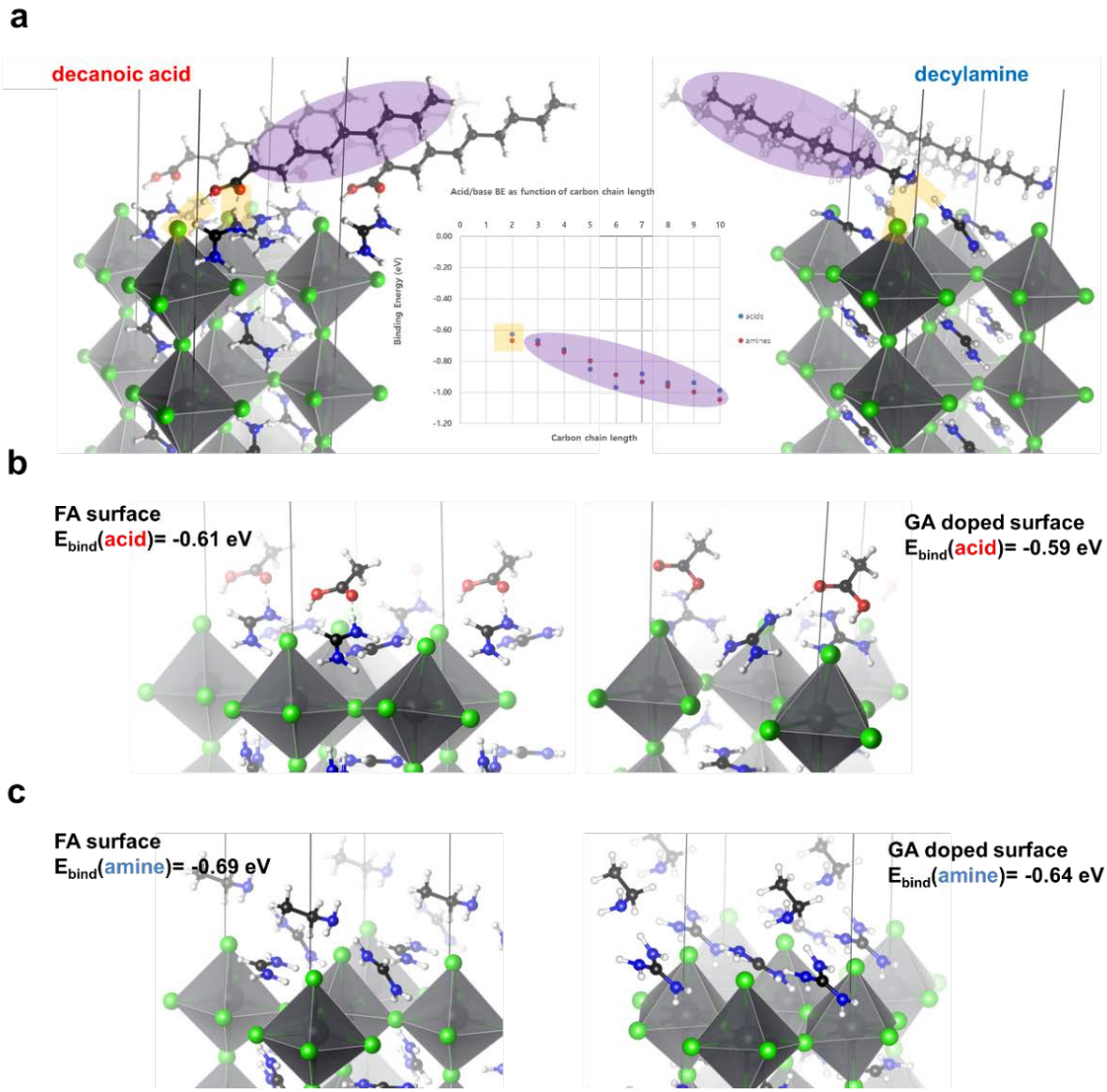

Supplementary Fig. 9 | Interaction of acids and amines with FABr or GABr terminated surface. a, Interaction of FABr terminated $FAPbBr_3$(001) surface with acids and amines with various alkyl length. Such interactions possess a local (point) chemical bonding component and a non-local van der Waals (vdW) component. We have used two colors in the plots to indicate the two type of interactions. **b, c,** Interaction of acetic acid (**b**) and ethylamine (**c**) with FABr terminated $FAPbBr_3$(001) surface and how it changes upon surface GA doping.

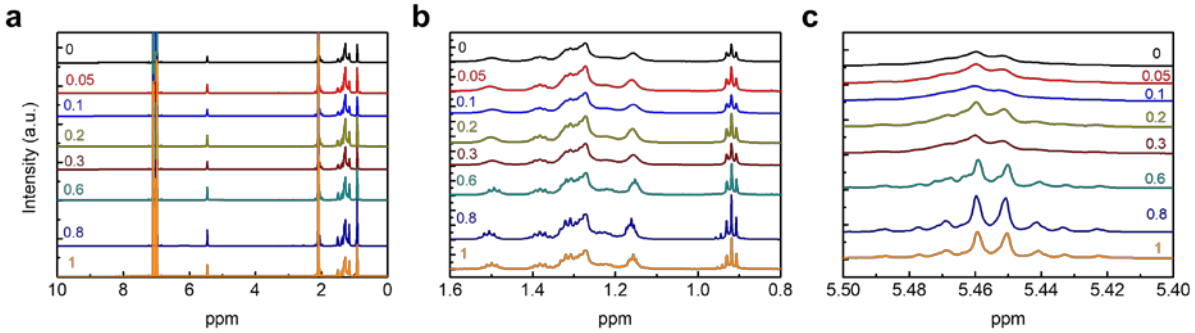

Supplementary Fig. 10 | Nuclear magnetic resonance (NMR) of $FA_{1-x}GA_xPbBr_3$ PNCs. a-c, NMR of $FA_{1-x}GA_xPbBr_3$ PNCs in the range of 0 to 10 ppm (**a**), 0.8 to 1.6 ppm (**b**) and 5.4 to 5.5 ppm (**c**).

As *x* increases, ^{1}H NMR spectrum show gradually sharpened resonance signals of organic ligands (at chemical shift (δ) ~1.3 ppm, ~1.52 ppm, ~5.45 ppm). Sharpening of the resonance signal is a result of weakened binding[25–27]; therefore, we conclude that surface covering GA stabilizes the surface internally and decreases its reactivity and interaction with external agents (organic ligands).

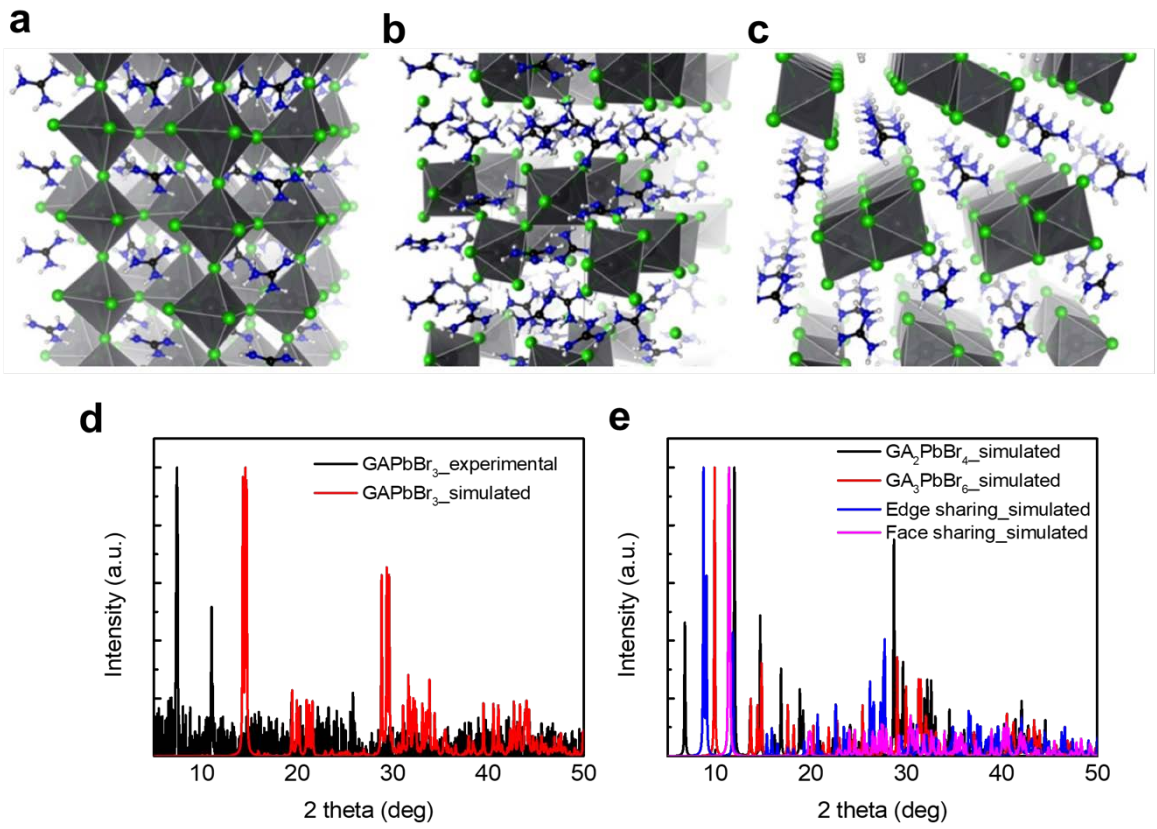

Supplementary Fig. 11 | DFT-derived crystal structures for different phases of guanidinium bromoplumbates. a-c, DFT-derived crystal structures for different phases of guanidinium bromoplumbates of the perovskite (3D corner sharing) $GAPbBr_3$ phase **(a)**, the GA_2PbBr_4 phase which is corner sharing and has 2D connectivity **(b)** and the edge sharing $GAPbBr_3$ phase with 1D connectivity **(c)**. Green: Br; gray within octahedra: Pb; white: H; blue: N; black: C. **d, e,** Comparing the experimental XRD pattern for *x*=1 guanidinium lead bromide with simulated XRD pattern for the corner-sharing perovskite phase **(d)** and other simulated XRD pattern for other phases of guanidinium lead bromide **(e)**.

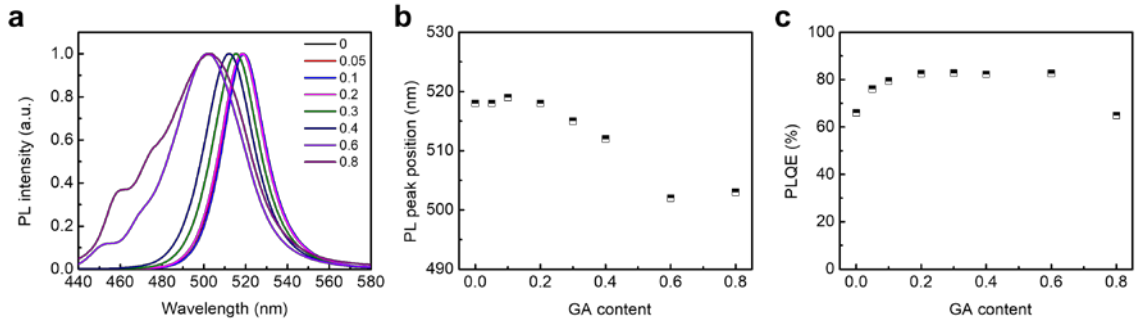

Supplementary Fig. 12 | PL characteristics of $MA_{1-x}GA_xPbBr_3$ PNCs. a-c, PL spectrum (**a**), PL peak wavelength (**b**) and PLQE (**c**) of $MA_{1-x}GA_xPbBr_3$ PNCs.

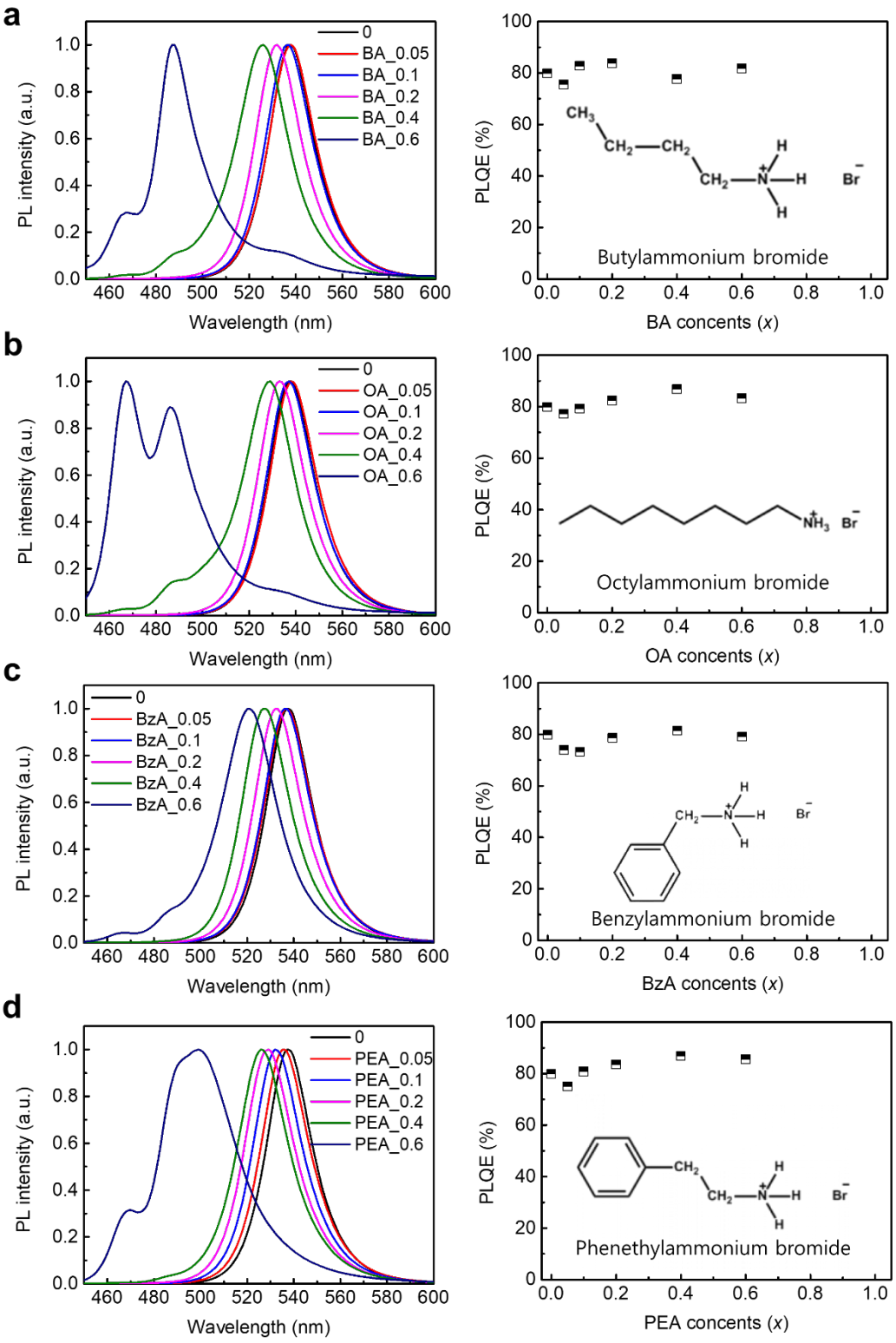

Supplementary Fig. 13 | PL spectrum and PLQE of PNCs with various bulky ammonium. **a-d,** PL spectrum (left) and PLQE (right) of $FA_{1-x}BA_xPbBr_3$ PNCs **(a)**, $FA_{1-x}OA_xPbBr_3$ PNCs **(b),** $FA_{1-x}BzA_xPbBr_3$ PNCs **(c)** and $FA_{1-x}PEA_xPbBr_3$ PNCs **(d)**. Here, BA is butylammonium, OA is octylammonium, BzA is benzylammonium and PEA is phenethylammonium.

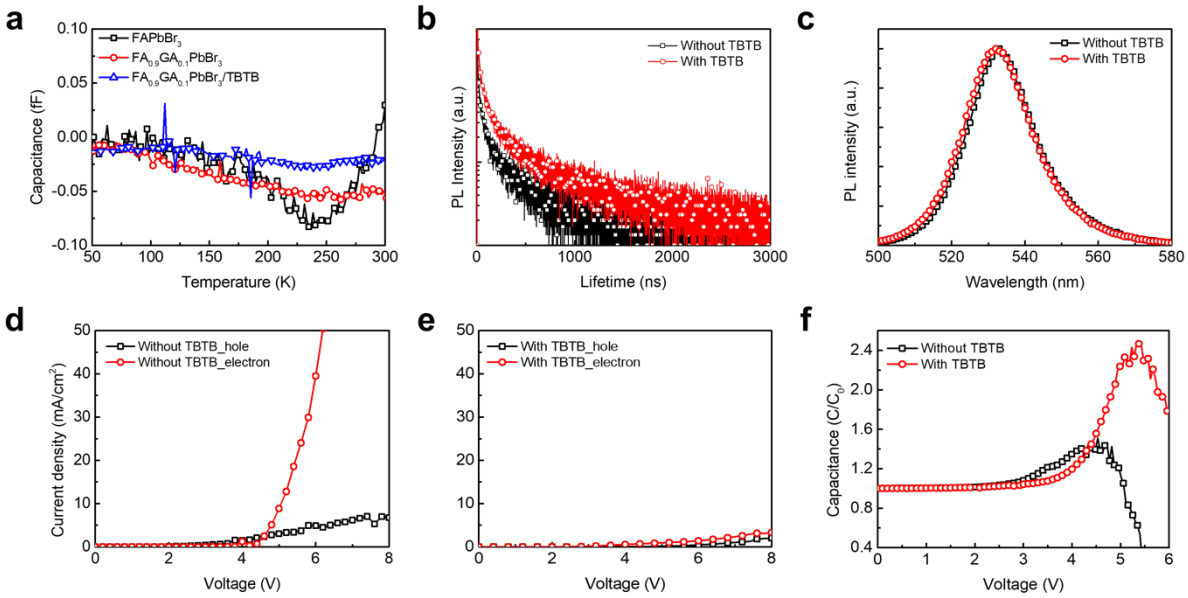

Supplementary Fig. 14 | Analysis of TBTB interlayer on the PNC films. a, Deep-level transient spectroscopy (DLTS) data of PeLEDs based on $FAPbBr_3$ and $FA_{0.9}GA_{0.1}PbBr_3$ PNCs without and with TBTB interlayer. **b, c,** PL lifetime **(b)** and PL spectrum **(c)** of $FA_{0.9}GA_{0.1}PbBr_3$ PNC films without and with TBTB interlayers. **d, e,** Electron-current densities and hole-current densities of electron-only and hole-only devices without (**d**) and with (**e**) TBTB interlayers. **f,** Capacitance-versus-voltage characteristics of PeLEDs based on $FA_{0.9}GA_{0.1}PbBr_3$ PNCs without and with TBTB interlayers.

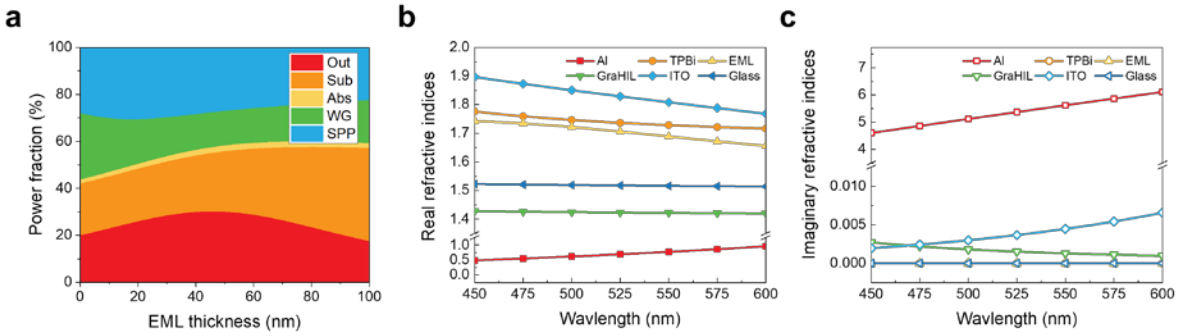

Supplementary Fig. 15 | Optical simulation of PeLEDs and refractive indices of materials used in the optical simulation. a, Simulated power fraction of each optical mode as a function of EML thickness (Out: out-coupling mode, Sub: substrate mode, Abs: absorption mode, WG: waveguide mode, SPP: surface plasmon mode). The device structure used in the simulation is Glass/ITO(70nm)/Buf-HIL(45nm)/EML(50nm)/TBTB(5nm)/ TPBI(50nm)/ Al(100nm). Only radiative contribution is presented because internal quantum efficiency was set to be unity. **b,** Real part of refractive indices. **c,** Imaginary part of refractive indices. We took absolute value of the refractive index of EML as a real refractive index since the fitting process of spectroscopic ellipsometry conserves magnitude of dielectric constants.

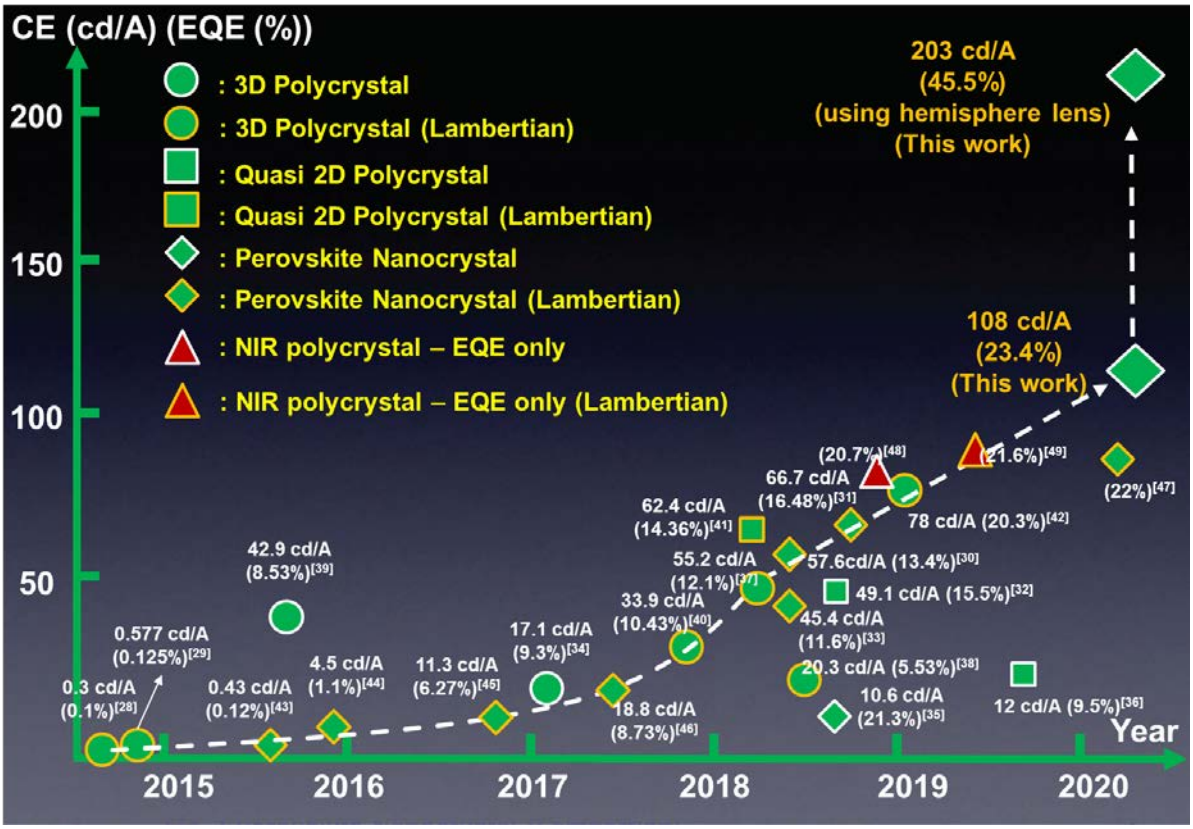

Supplementary Fig. 16 | Progress of current efficiencies (CEs) and external quantum efficiencies (EQEs) in PeLEDs. Progress of CEs and EQEs in visible PeLEDs based on perovskite polycrystalline (PPC) bulk films and nanocrystals (PNCs)[28–47] and EQEs in near-infrared PeLEDs[48,49].

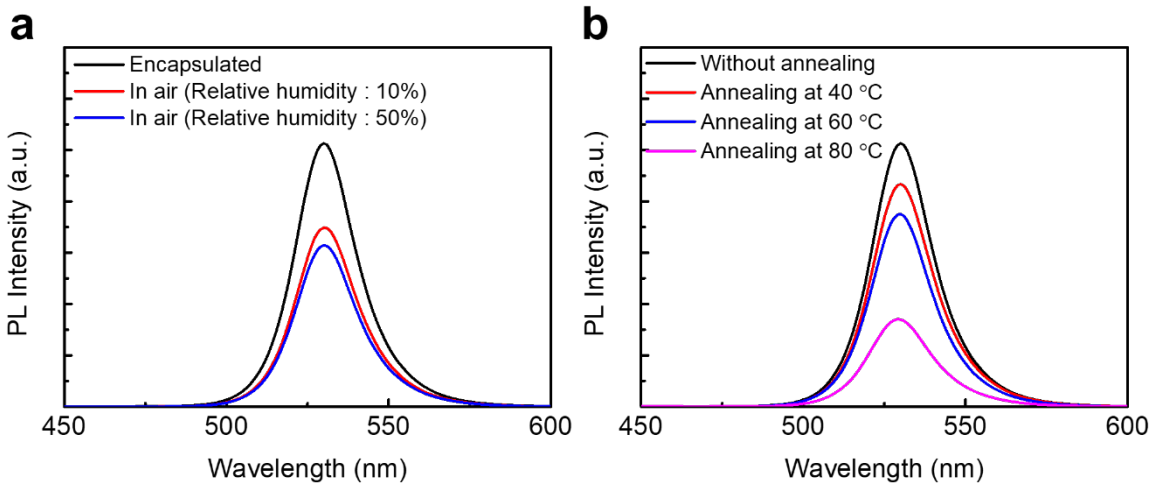

Supplementary Fig. 17 | PL spectra of $FA_{0.9}GA_{0.1}PbBr_3$ PNC films under different conditions. a, b, PL spectra of $FA_{0.9}GA_{0.1}PbBr_3$ PNC films under various environmental conditions (**a**) and with different thermal annealing temperatures (**b**).

We also measured the device lifetime of the PeLEDs based on $FA_{0.9}GA_{0.1}PbBr_3$ PNCs under various current injection, moisture and heat conditions. As per the **Fig. 6b**, these experiments indicate a gradually decreasing device lifetime as the applied current (initial measurement luminance) increases: from T_{50} = 132 min at 0.009 mA (100 cd/m^2) to T_{50} = 7 min at 0.053 mA (1000 cd/m^2). Such a decrease (with increasing driving current) can be accelerated by the induced ion-migration and ion-migration-induced defects inside the perovskite layer caused by the sizable electric field across the device[50]. The ion-migration-induced device deterioration is confirmed by fast change of driving voltage under the high electric field (inset of **Fig. 6b**)[51].

PeLEDs showed dramatically reduced device lifetimes in air (T_{50} = 8 min under 10% relative humidity, T_{50} = 3 min under 50% relative humidity) than PeLEDs encapsulated with a cover glass which maintains the nitrogen condition (T_{50} = 132 min) (**Fig. 6c**). To investigate the reason for the significant decrease of device lifetime in air, we measured the PL spectrum of $FA_{0.9}GA_{0.1}PbBr_3$ PNC films in encapsulation and in air under different relative humidity

(**Supplementary Fig. 17a**). The $FA_{0.9}GA_{0.1}PbBr_3$ PNC films still showed high PL intensity in air, which is slightly reduced compared to the PNC films in encapsulation. Therefore, we attribute the dramatically decreased device lifetime in air mainly to reaction between the oxygen gas and LiF (electron injecting material) in the PeLEDs. Also, our devices showed gradually decreasing lifetime as the thermal annealing temperature of PNC films increased (from T_{50} = 132 min without annealing to T_{50} = 16 min with annealing at 80 ºC for 10 min) (**Fig. 6d**). Such annealing can induce defects or aggregation in PNCs and reduce the luminescence efficiency: these are confirmed by decreasing PL intensity of $FA_{0.9}GA_{0.1}PbBr_3$ PNC films annealed at various temperatures (**Supplementary Fig. 17b**).

Supplementary Table 1. Size, size distribution and calculated number of atoms in $FA_{1-x}GA_xPbBr_3$ PNCs by assuming that PNCs are cubic shape.

Sample	$x = 0$	$x = 0.05$	$x = 0.1$	$x = 0.2$	$x = 0.3$	$x = 0.6$	$x = 0.8$
Mean size (nm)	10.04914	9.633793	8.759448	8.287241	7.328621	6.745862	5.095862
Standard deviation (nm)	1.644652	0.940252	1.47802	1.392435	1.569588	1.345016	1.330248
number of cations (total)	4698.213	4139.408	3111.548	2634.973	1822.271	1421.211	612.6314
number of cations (in surface)	1683.086	1546.833	1278.799	1144.639	895.1447	758.4443	432.7968
surface/total A-cation ratio	0.35824	0.373685	0.410985	0.434403	0.491225	0.53366	0.706456
number of GA cations (total)	0	206.9704	311.1548	526.9947	546.6813	852.7267	490.1051
number of GA cations on surface (by guessing 10% of GA are added into the bulk area)	0	77.34164	127.8799	377.9613	453.9687	786.45	472.1217

Indeed, getting closer to x=1, renders the perovskite phase unstable. As per the Supplementary Table 1, such particles do not have a significant crystalline bulk region (due to small size) and the (inhomogeneous) surface tension effects, induced by the binding ligands, renders such perovskite PNCs amorphous-like (loss of the XRD peaks), featuring a large surface to bulk ratio (smaller sizes) and fully-covered GA shell. Nevertheless, the perovskite PNCs with x>0.6 can still be synthesized. One should note that, for x=0.8, we still observe perovskite signature in the PL spectrum (peak ~ 510 nm), which is due to existence of some $PbBr_6$ octahedra in these particles.

Supplementary Table 2. Calculated defect parameters (activation energy and density) in $FA_{1-x}GA_xPbBr_3$ PNC films without and with a TBTB interlayer.

Samples	Defect activation energy (eV)	Defect density (N_t (cm^{-3}))
$FAPbBr_3$	≈0.5	4.93×10^{12}
$FA_{0.9}GA_{0.1}PbBr_3$	≈0.5	3.10×10^{12}
$FA_{0.9}GA_{0.1}PbBr_3$/TBTB	≈0.5	1.70×10^{12}

Supplementary Table 3. Highest EL efficiencies of our devices, previously reported visible and near-infrared (NIR) PeLEDs based on PNCs and polycrystalline (PPC) bulk films, and quantum dot (QD) LEDs.

Device	**Our work**	**Green PNC PeLED**[47]	**Red PNC PeLED**[35]	**NIR PPC PeLED**[49]	**Green PPC PeLED**[42]	**NIR PPC PeLED**[48]	**Green QD LEDs**[52]	**Red QD LEDs**[53]
Max CE ($cd \cdot A^{-1}$)	108	n/a	10.6	n/a	78	n/a	98.2	30
Max EQE (%)	23.4	22	21.3	21.6	20.3	20.7	24.8	21.6
CE/EQE ratio	4.62	n/a	0.50	n/a	3.84	n/a	3.96	1.39
EL peak wavelength (nm)	531	~510	653	800	525	803	522	≈615
EQE calculation	Angular emission	n/a	Angular emission	n/a	Lambertian assumption	Angular emission	n/a	Angular emission

Our device efficiencies are compared with the those of PeLEDs based on PNCs and PPCs, and QD LEDs in references[35,42,47,48,49,52,53].

Lambertian assumption can induce inaccurate calculation of the EQE values[54,55], therefore comparing CE values are more correct and reliable when luminance is measured by spectroradiometer without considering angular EL distribution.

Supplementary Table 4. Reported EL efficiencies inorganic quantum dot (QD) light-emitting diodes

Publication date(ref)	Emission layer (Emission color, Wavelength)	Device structure	EL efficiencies (current efficiency (CE), external quantum efficiency (EQE))
1994/08[56]	PPV[a]:CdSe (yellow, peak ~520, ~550, ~600 nm)	ITO/QDs/PPV/Mg	EQE ~0.001-0.01%
2002/12[57]	CdSe/ZnS (green, 562 nm)	ITO/TPD[b]/QDs/Alq_3[c]/Mg:Ag/Ag	CE ~ 1.9 cd/A, EQE ~ 0.52%
2003/09[58]	CdSe/ZnS (red, ~635 nm)	ITO/TPD/QDs/TAZ[d]/Alq_3/Mg:Ag/ Ag	EQE ~ 1.1%
2003/11[59]	PbSe (NIR, 1.2 μm-2.2 μm)	ITO/TPD or α-NPD[e]/QDs/Alq_3/BCP[f]/Mg:Ag/Ag	EQE ~ 0.001%
2006/07[60]	$Cd_xZn_{1-x}Se/Cd_yZn_{1-y}S$ (green, 520 nm)	ITO/CBP[g]/QDs/TAZ/Alq_3/Mg:Ag/ Ag	EQE ~ 0.5%
2006/09[61]	CdSe/ZnS (white)	ITO//PEDOT:PSS[h]/CBP:QDs/Alq_3 /Ca/Al	CE ~ 2.2 cd/A
2007/07[62]	ZnCdS (blue, ~440 nm) ZnSe/CdSe/ZnS (green, ~540 nm) CdSe/ZnS (red, ~620 nm)	ITO/PEDOT:PSS/TPD/QDs/TAZ/ Alq_3/ Mg:Ag/Ag	Blue: EQE ~ 0.35% Green: EQE ~ 0.65% Red: EQE ~ 1.6% White: EQE ~ 0.36%
2007/09[63]	CdSe/CdS (red, ~610 nm) CdSe/CdZnS/ZnS (red, ~593 nm)	ITO/PEDOT:PSS/BiVB-MeTPD[l]/ QDs/TPBI/CsF/Al	CE ~ 4.21 cd/A, EQE ~ 2.12% CE ~ 4.87 cd/A, EQE ~ 1.74%
2007/12[64]	CdSe/ZnS (green, 525 nm) CdSe/ZnS (yellow, 576 nm) CdSe/CdS/ZnS (orange, 595 nm) CdSe/CdS/ZnS (red, 619 nm)	ITO/PEDOT:PSS/Poly-TPD[m]/ QDs/Alq_3/Ca/Al	Green: CE ~ 1.1 cd/A Yellow: 1.3 cd/A Orange: 1.8 cd/A Red: 2.8 cd/A
2008/03[65]	ZnCdSe (red, 642 nm)	ITO/NiO/QDs/ZnO:SnO_2/Ag	CE ~ 0.064 cd/A, EQE ~ 0.09%
2008/11[66]	CdS/ZnS (blue, ~460 nm) ZnSe/CdSe/ZnS (green, ~520 nm)	ITO/PEDOT:PSS/TPD/QDs/TAZ/ Alq_3/ Mg:Ag/Ag	Blue: EQE ~ 0.2% Green: EQE ~ 0.5% Red: EQE ~ 1.0%

	CdSe/ZnS (red, ~610 nm)		
2009/06[67]	ZnCdS/ZnS (blue, ~460 nm) ZnCdS (cyan, ~490 nm) ZnSe/CdSe/ZnS (green, ~545 nm) CdSe/ZnS (orange, ~600 nm) CdZnSe (red, ~650 nm)	ITO/spiro-TPD[n]/QDs/TPBI[o]/Mg:Ag/Ag	Blue: EQE ~ 0.4% Cyan: EQE ~ 0.2% Green: EQE ~ 2.6% Orange: EQE ~ 2.7% Red: EQE ~ 1.0%
2009/06[68]	CdSe/CdS/ZnS (red, 618 nm)	ITO/PEDOT:PSS/TFB[p]/QDs/TiO_2/Al	CE ~ 2.53 cd/A, EQE ~ 1.5%
2009/12[69]	CdSe/ZnS (red, ~628 nm)	ITO/ZnO/QDs/alloyed ZnO and SnO_2/ITO	CE ~ 2 cdA, EQE ~ 0.15%
2011/03[70]	CdS/ZnS (blue, 480 nm) CdSe/CdS/ZnS (green, 530 nm) CdSeS/ZnS (red, 615 nm)	ITO/PEDOT:PSS/TFB/QDs/TiO_2/Al	Blue: CE ~ 0.04 cd/A Green: CE ~ 0.5 cd/A Red: CE ~ 4 cd/A
2011/09[71]	InP/ZnSeS (green, 532 nm)	ITO/PEDOT:PSS/Poly-TPD /QDs/TPBI/LiF/Al	EQE ~ 0.008%
2012/04[72]	CdSe/ZnS (blue, 437 nm green, 520 nm red, 637 nm)	ITO/ZnO/QDs/CBP/MoO_3/Al (blue: $Cd_{1-x}Zn_xS$/ZnS green: CdSe/ZnS red: CdSe/CdS/ZnS)	Blue: CE ~ 0.4 cd/A, EQE ~ 1.7% Green: CE~ 19.2 cd/A, EQE ~ 5.8% Red: 5.7 cd/A, EQE ~ 7.3%
2012/11[73]	CdSe/CdS/ZnS (red, ~628 nm)	ITO/Al:ZnO/QDs/TCTA[q]/NPD/HATCN[r]/Al	CE ~ 5.21 cd/A
2013/05[74]	CdSe/CdS (red, ~615 nm)	ITO/ZnO/QDs/NPB/spiro-2NPB[s]/LG-101/Al	CE ~ 19 cd/A, EQE ~ 18%
2013/11[75]	CdSe/CdS/ZnS (white)	ITO/PEDOT:PSS/TFB/QDs/TiO_2/Al	CE ~ 0.44 cd/A
2014/04[76]	CdSe@ZnS/ZnS (red, ~516 nm)	ITO/PEDOT:PSS/PVK[t]/QDs/ZnO/Al	CE ~ 46.4 cd/A, EQE ~ 12.6%
2014/10[77]	CdSe/CdS (red, ~640 nm)	ITO/PEDOT:PSS/Poly-TPD /PVK/QDs/PMMA[u]/ZnO/Ag	EQE ~ 20.5%
2014/11[78]	$CdSe/Zn_{1-x}Cd_xS$ (red, ~626 nm)	ITO/ZnO/QDs/CBP/MoO_x/Al	EQE ~ 7.4%
2015/03[79]	$Cd_{1-x}Zn_xSe_{1-y}S_y$ (blue, 455 nm green, 537 nm red, 625 nm)	ITO/PEDOT:PSS/TFB/QDs/ZnO/Al	Blue: CE ~ 4.4 cd/A, EQE ~ 10.7% Green: CE ~ 63 cd/A, EQE ~ 14.5% Red: CE ~ 15 cd/A, EQE ~ 12%

2016/02[80]	PbS (NIR, 1,391nm)	ITO/TiO_2/$MAPbI_xBr_{3-x}$:QDs/$F8^v$/MoO_3/Ag	EQE ~ 5.2%
2016/12[81]	$Cd_{1-x}Zn_xS$/ZnS (blue, 445 nm) CdCd1−*x*Zn*x*Se/ZnS (green, 520 nm) CdSe/Cd1−*x*Zn*x*S (red, 628 nm)	ITO/ZnO/QDs/CBP/MoO_x//Al	Blue: CE ~ 0.22 cd/A, EQE ~ 0.91% Green: CE~13.43 cd/A, EQE ~ 3.94% Red: 6.99 cd/A, EQE ~ 7.12%
2017/02[82]	CdSe@ZnS/ZnS (green, ~528 nm)	ITO/ZnO/QDs/$PEIE^w$/Poly-TPD/MoO_x/Al	CE ~ 65.3 cd/A, EQE ~ 15.6%
2017/04[83]	CdSe/ZnS (green, 528 nm)	ITO/PEDOT:PSS/$SDTF^x$/QDs/ZnO/Al	CE ~ 22.82 cd/A, EQE ~5.54%
2018/02[84]	CdSeZnS:Cl/ZnS (green, ~520 nm)	ITO/ZnO/QDs/CBP/MoO_x/Al	CE ~ 20 cd/A, EQE ~ 6%
2018/07[85]	CdSe/$Cd_{1-x}Zn_xSe$/ZnSe (red, 631 nm)	ITO/PEDOT:PSS/TFB/QDs/ZnO/Al	CE ~ 15.9 cd/A, EQE ~ 15.1%
2018/09[86]	CdSe/$Cd_xZn_{1-x}Se$/$ZnSe_yS_{1-y}$ (orange, ~610 nm)	ITO/ZnO:PVP/QDs/TCTA/MoO_x/Al	EQE ~ 13.5%
2019/02[53]	CdSe/ZnS (green, ~530 nm) CdSe/ZnCdSe/ZnSe (red, ~615 nm) $Zn_xCd_{1-x}Se$/ZnSe (blue, ~480 nm)	ITO/PEDOT:PSS/TFB/QDs/ZnO/Al	Blue: EQE ~ 8.05% Green: CE ~ 90 cd/A, EQE ~ 22.9% Red: CE ~ 30 cd/A, EQE ~ 21.6%
2019/04[87]	CdSe/ZnS (red, 620 nm)	ITO/PEDOT:PSS/PVK/QDs/GA:ZnO/Ag	CE ~ 15 cd/A
2019/04[88]	InP/ZnSe/ZnS (red, 630 nm)	ITO/PEDOT:PSS/Poly-TPD /QDs/$Zn_{0.9}Mg_{0.1}O$/Ag	CE ~ 14.7 cd/A, EQE ~ 12.2%
2019/10[89]	Ag_2S@SiO_2 (NIR, 1404 nm)	ITO/TiO_2/$MA_xFA_yCs_{1-x-y}Pb(Br_zI_{1-z})_3$:QDs/porphyrin/$MoO_x$/Ag	EQE ~ 16.98%
2019/10[90]	ZnCdSe/ZnSe/ZnSeS/ZnS (green, 531 nm)	ITO/PEDOT:PSS/TFB/QDs/ZnO NPs/Al	CE ~ 100.5 cd/A. EQE ~ 23.9%
2019/11[52]	CdSe@ZnS/ZnS (green, ~522 nm)	ITO/ZnO/QDs/PEIE/Poly-TPD/MoO_x/Al	CE ~ 98.2 cd/A, EQE ~ 24.8%
2019/11[91]	InP/ZnSe/ZnS (red, 630 nm)	ITO/PEDOT:PSS/TFB/QDs/ZnMgO/Al	Red: EQE ~ 21.4%
2019/11[52]	CdSe@ZnS/ZnS (green, 522 nm)	ITO/ZnO NPs^y/QDs/PEIE/poly-TPD^m/MoO_x/Al	CE ~ 98.2 cd/A, EQE ~ 24.8%
2019/11[92]	CdSe/CdZnSe/ZnSeS (red, 625 nm)	ITO/BA-CF_3^z modified NiO/poly-TPD/TFB/QDs/$Zn_{0.9}Mg_{0.1}O$/Ag	CE ~ 19.4 cd/A, EQE ~ 13.4%
2020/04[93]	CdZnSe/ZnS (red, 636 nm)	ITO/PEDOT:PSS/TFB/QDs/MgO@ZnO NPs/Al	CE ~ 22.4 cd/A, EQE ~ 20.6%

2020/04[94]	CdSe/$Cd_{1-x}Zn_xSe$/ZnSe (red, ~630 nm)	ITO/Nissan HIL/TFB/QDs/ZnO NPs/Al	EQE ~ 16.6%
2020/05[95]	CdSe/CdZnSe/ZnSeS (green, 522 nm)	ITO/PEDOT:PSS/TFB/QDs/$Zn_{0.9}Mg_{0.1}O$/Ag	EQE ~ 20.1%

[a]PPV: p-paraphenylene nivylene; [b]TPD: N,N′-Bis(3-methylphenyl)-N,N′-diphenylbenzidine; [c]Alq_3: Tris-(8-hydroxyquinoline)aluminum; [d]TAZ: 4-biphenyllyl)-4-p henyl-5-tert-butylphenyl-1,2,4-triazole; [e]α-NPD: N,N'-bis(1-naphthyl)-N,N'-diphenyl-1,1'-biphenyl-4,4'-diamine; [f]BCP: Bathocuproine; [g]CBP: 4,4′-bis(Ncarbazolyl)-1,1′-biphenyl; [h]PEDOT:PSS: Poly(3,4-ethylenedioxythiophene)-poly(styrenesulfonate); [l]BiVB-MeTPD: bivinylbenzylether methyl-tetraphenylbiphenyldiamine; [m]Poly-TPD: Poly(N,N'-bis-4-butylphenyl-N,N'-bisphenyl)benzidine; [n]spiro-TPD: spiro-N,N′-diphenyl-N,N′-bis(3-methylphenyl)-(1,1′-biphenyl)-4,4′-diamine; [o]TPBI: 2,2',2''-(1,3,5-Benzinetriyl)-tris(1-phenyl-1-H-benzimidazole); [p]TFB: poly[(9,9-dioctylfluorenyl-2,7-diyl)-co-(4,4′-(N-(4-sec-butylphenyl))diphenylamine)]; [q]TCTA: 4,4',4''-Tri(N-carbazolyl)triphenylamine; [r]HATCN: Dipyrazino[2,3-f:2’,3’-h]quinozaline-2,3,6,7,10,11-hexacarbonitrile; [s]spiro-2NPB: 2,2’,7,7’-tetrakis[N-naphthalenyl(phenyl)-amino]-9,9-spirobifluorene; [t]PVK: poly(9-vinylcarbazole); [u]PMMA: poly(methylmethacrylate); [v]F8: poly(9,9’-dioctylfluorene); [w]PEIE: polyethylenimine ethoxylated; [x]SDTF: N,N′-(9,9′-spirobi-[fluorene]-2,7-diylbis[4,1-phenylene])bis(N-phenyl-4′-vinyl-[1,1′-biphenyl]-4-amine); [y]NPs: nanoparticles; [z]BA-CF_3:4-(trifluoromethyl)benzoic acid

Supplementary Table 5. a, Elastic coefficients from C_{11} to C_{66}

	C_{11}	C_{22}	C_{33}	C_{23}	C_{13}	C_{12}	C_{44}	C_{55}	C_{66}
FA_1GA_0	25.98	26.43	39.94	9.76	9.25	19.82	4.75	4.03	15.15
$GA_{0.125\_(2*2*2)}$	36.87	34.33	38.51	10.71	9.22	8.69	4.13	4.03	3.31
$FA_{0.75}GA_{0.25}$	26.27	27.13	38.12	10.08	10.53	19.70	4.84	3.97	14.50
$FA_{0.50}GA_{0.50}$	24.07	24.09	37.79	11.01	9.05	15.95	4.67	5.59	10.91
$FA_{0.25}GA_{0.75}$	31.32	22.03	16.11	7.16	7.43	20.23	4.99	4.33	14.80
FA_0GA_1	29.06	24.71	16.58	8.54	9.33	16.68	6.49	4.01	13.80
GA_2PbBr_4	17.17	18.23	21.66	9.48	12.09	10.34	5.28	6.93	5.23
$GA_{e\text{-}phase}$	14.77	15.58	27.73	8.30	14.56	8.34	2.85	4.78	4.85

b, Elastic coefficients from C_{14} to C_{56}

C_{14}	C_{15}	C_{16}	C_{24}	C_{25}	C_{26}	C_{34}	C_{35}	C_{36}	C_{45}	C_{46}	C_{56}
0	1.10	-0.25	0	-0.67	0	-0.60	-0.99	-0.89	0	-0.76	-0.47
0	-0.77	0.27	0	0.77	-0.43	0	-0.45	0	-0.50	0.62	0
0.93	0.30	-0.49	-0.77	-0.48	0.29	-0.37	0.30	1.12	0.36	-0.33	0.70
1.07	0	0	0	0	0	3.21	0	0	0	0	0.45
2.42	-0.95	0.99	-0.48	0.21	0	1.91	0.68	0.88	0.93	0	1.74
2.47	-0.59	-0.37	2.94	-0.40	-0.60	3.02	0.50	0.55	0	0	2.14
-0.22	-2.8	-0.3	0	-0.42	0	0	-3.25	0	0	0.74	0
0	0	0	0	0	0	0	0	0	0	0	0

Unit: GPa

Supplementary Table 6. Effective elastic moduli

	B_V	B_R	B_{VRH}	B_V error
FA_1GA_0	18.89	18.83	18.86	0.23
$GA_{0.125\ (2*2*2)}$	18.55	18.49	18.52	0.28
$FA_{0.75}GA_{0.25}$	19.13	19.11	19.12	0.26
$FA_{0.50}GA_{0.50}$	17.55	16.98	17.27	0.36
$FA_{0.25}GA_{0.75}$	15.46	12.40	13.93	0.21
FA_0GA_1	15.49	12.31	13.90	0.20
GA_2PbBr_4	13.43	12.67	13.05	0.22
$GA_{e\text{-}phase}$	13.39	11.74	12.57	0.12

Unit: GPa

References

1. Nielsen, O. H. & Martin, R. M. First-principles calculation of stress. *Phys. Rev. Lett.* **50**, 697–700 (1983).
2. Caro, M. A., Schulz, S. & O'Reilly, E. P. Comparison of stress and total energy methods for calculation of elastic properties of semiconductors. *J. Phys. Condens. Matter* **25**, 025803 (2013).
3. De Jong, M. *et al.* Charting the complete elastic properties of inorganic crystalline compounds. *Sci. Data* **2**, 150009 (2015).
4. Brugger, K. Determination of third-order elastic coefficients in crystals. *J. Appl. Phys.* **36**, 768–773 (1965).
5. Den Toonder, J. M. J., Van Dommelen, J. A. W. & Baaijens, F. P. T. Relation between single crystal elasticity and the effective elastic behaviour of polycrystalline materials: Theory, measurement and computation. *Model. Simul. Mater. Sci. Eng.* **7**, 909–928 (1999).
6. Faghihnasiri, M., Izadifard, M. & Ghazi, M. E. DFT study of mechanical properties and stability of cubic methylammonium lead halide perovskites ($CH_3NH_3PbX_3$, X = I, Br, Cl). *J. Phys. Chem. C* **121**, 27059–27070 (2017).
7. Mouhat, F. & Coudert, F. X. Necessary and sufficient elastic stability conditions in various crystal systems. *Phys. Rev. B* **90**, 224104 (2014).
8. Reuter, K., Stampf, C. & Scheffler, M. *AB initio atomistic thermodynamics and statistical mechanics of surface properties and functions*. in *Handbook of Materials Modeling: Methods* (ed. Yip, S.) 149–194 (Springer Netherlands, 2005). doi:10.1007/978-1-4020-3286-8_10.
9. Huang, X., Paudel, T. R., Dowben, P. A., Dong, S. & Tsymbal, E. Y. Electronic structure and stability of the $CH_3NH_3PbBr_3$ (001) surface. *Phys. Rev. B* **94**, 195309 (2016).

10. Shi, T., Yin, W. J., Hong, F., Zhu, K. & Yan, Y. Unipolar self-doping behavior in perovskite $CH_3NH_3PbBr_3$. *Appl. Phys. Lett.* **106**, 103902 (2015).

11. Teng, Q., Shi, T. T., Tian, R. Y., Yang, X. B. & Zhao, Y. J. Role of organic cations on hybrid halide perovskite $CH_3NH_3PbI_3$ surfaces. *J. Solid State Chem.* **258**, 488–494 (2018).

12. Yin, W.-J., Shi, T. & Yan, Y. Unusual defect physics in $CH_3NH_3PbI_3$ perovskite solar cell absorber. *Appl. Phys. Lett.* **104**, 063903 (2014).

13. Haruyama, J., Sodeyama, K., Han, L. & Tateyama, Y. Termination dependence of tetragonal $CH_3NH_3PbI_3$ surfaces for perovskite solar cells. *J. Phys. Chem. Lett.* **5**, 2903–2909 (2014).

14. Kabakova, I. V. *et al.* The effect of ionic composition on acoustic phonon speeds in hybrid perovskites from Brillouin spectroscopy and density functional theory. *J. Mater. Chem. C* **6**, 3861–3868 (2018).

15. Quarti, C., De Angelis, F. & Beljonne, D. Influence of surface termination on the energy level alignment at the $CH_3NH_3PbI_3$ perovskite/C_{60} interface. *Chem. Mater.* **29**, 958–968 (2017).

16. She, L., Liu, M. & Zhong, D. Atomic structures of $CH_3NH_3PbI_3$ (001) surfaces. *ACS Nano* **10**, 1126–1131 (2016).

17. Liu, Y. *et al.* Atomistic origins of surface defects in $CH_3NH_3PbBr_3$ perovskite and their electronic structures. *ACS Nano* **11**, 2060–2065 (2017).

18. Hieulle, J. *et al.* Unraveling the impact of halide mixing on perovskite stability. *J. Am. Chem. Soc.* **141**, 3515–3523 (2019).

19. Kakekhani, A. *et al.* Nature of lone-pair–surface bonds and their scaling relations. *Inorg. Chem.* **57**, 7222–7238 (2018).

20. Fan, Z. *et al.* Layer-by-layer degradation of methylammonium lead tri-iodide perovskite

microplates. *Joule* **1**, 548–562 (2017).

21. Mosconi, E., Azpiroz, J. M. & De Angelis, F. *Ab initio* molecular dynamics simulations of methylammonium lead iodide perovskite degradation by water. *Chem. Mater.* **27**, 4885–4892 (2015).

22. Brenes, R. *et al.* Metal halide perovskite polycrystalline films exhibiting properties of single crystals. *Joule* **1**, 155–167 (2017).

23. Galisteo-López, J. F., Anaya, M., Calvo, M. E. & Míguez, H. Environmental effects on the photophysics of organic-inorganic halide perovskites. *J. Phys. Chem. Lett.* **6**, 2200–2205 (2015).

24. Cohen, A. V, Egger, D. A., Rappe, A. M. & Kronik, L. Breakdown of the static picture of defect energetics in halide perovskites: The case of the Br vacancy in $CsPbBr_3$. *J. Phys. Chem. Lett.* **10**, 4490–4498 (2019).

25. Fritzinger, B., Capek, R. K., Lambert, K., Martins, J. C. & Hens, Z. Utilizing self-exchange to address the binding of carboxylic acid ligands to CdSe quantum dots. *J. Am. Chem. Soc.* **132**, 10195–10201 (2010).

26. Zeng, B. *et al.* Characterization of the ligand capping of hydrophobic CdSe–ZnS quantum dots using NMR spectroscopy. *Chem. Mater.* **30**, 225–238 (2018).

27. De Roo, J. *et al.* Highly dynamic ligand binding and light absorption coefficient of cesium lead bromide perovskite nanocrystals. *ACS Nano* **10**, 2071–2081 (2016).

28. Tan, Z.-K. *et al.* Bright light-emitting diodes based on organometal halide perovskite. *Nat. Nanotechnol.* **9**, 687–692 (2014).

29. Kim, Y.-H. *et al.* Multicolored organic/inorganic hybrid perovskite light-emitting diodes. *Adv. Mater.* **27**, 1248–1254 (2015).

30. Chin, X. Y. *et al.* Self-assembled hierarchical nanostructured perovskites enable highly efficient LEDs *via* an energy cascade. *Energy Environ. Sci.* **11**, 1770–1778 (2018).

31. Song, J. *et al.* Organic–inorganic hybrid passivation enables perovskite QLEDs with an EQE of 16.48%. *Adv. Mater.* **30**, 1805409 (2018).

32. Ban, M. *et al.* Solution-processed perovskite light emitting diodes with efficiency exceeding 15% through additive-controlled nanostructure tailoring. *Nat. Commun.* **9**, 3892 (2018).

33. Song, J. *et al.* Room-temperature triple-ligand surface engineering synergistically boosts ink stability, recombination dynamics, and charge injection toward EQE-11.6% perovskite QLEDs. *Adv. Mater.* **30**, 1800764 (2018).

34. Xiao, Z. *et al.* Efficient perovskite light-emitting diodes featuring nanometre-sized crystallites. *Nat. Photon.* **11**, 108–115 (2017).

35. Chiba, T. *et al.* Anion-exchange red perovskite quantum dots with ammonium iodine salts for highly efficient light-emitting devices. *Nat. Photon.* **12**, 681–687 (2018).

36. Liu, Y. *et al.* Efficient blue light-emitting diodes based on quantum-confined bromide perovskite nanostructures. *Nat. Photon.* **13**, 760–764 (2019).

37. Lee, S. *et al.* Growth of nanosized single crystals for efficient perovskite light-emitting diodes. *ACS Nano* **12**, 3417–3423 (2018).

38. Shi, Y. *et al.* A strategy for architecture design of crystalline perovskite light-emitting diodes with high performance. *Adv. Mater.* **30**, 1800251 (2018).

39. Cho, H. *et al.* Overcoming the electroluminescence efficiency limitations of perovskite light-emitting diodes. *Science* **350**, 1222–1225 (2015).

40. Zhang, L. *et al.* Ultra-bright and highly efficient inorganic based perovskite light-emitting diodes. *Nat. Commun.* **8**, 15640 (2017).

41. Yang, X. *et al.* Efficient green light-emitting diodes based on quasi-two-dimensional composition and phase engineered perovskite with surface passivation. *Nat. Commun.* **9**, 570 (2018).

42. Lin, K. *et al.* Perovskite light-emitting diodes with external quantum efficiency exceeding 20 per cent. *Nature* **562**, 245–248 (2018).

43. Song, J. *et al.* Quantum dot light-emitting diodes based on inorganic perovskite cesium lead halides ($CsPbX_3$). *Adv. Mater.* **27**, 7162–7167 (2015).

44. Huang, H. *et al.* Emulsion synthesis of size-tunable $CH_3NH_3PbBr_3$ quantum dots: an alternative route toward efficient light-emitting diodes. *ACS Appl. Mater. Interfaces* **7**, 28128–28133 (2015).

45. Li, J. *et al.* 50-Fold EQE improvement up to 6.27% of solution-processed all-inorganic perovskite $CsPbBr_3$ QLEDs *via* surface ligand density control. *Adv. Mater.* **29**, 1603885 (2017).

46. Chiba, T. *et al.* High-efficiency perovskite quantum-dot light-emitting devices by effective washing process and interfacial energy level alignment. *ACS Appl. Mater. Interfaces* **9**, 18054–18060 (2017).

47. Dong, Y. *et al.* Bipolar-shell resurfacing for blue LEDs based on strongly confined perovskite quantum dots. *Nat. Nanotechnol.* **15**, 668–674 (2020).

48. Cao, Y. *et al.* Perovskite light-emitting diodes based on spontaneously formed submicrometre-scale structures. *Nature* **562**, 249–253 (2018).

49. Xu, W. *et al.* Rational molecular passivation for high-performance perovskite light-emitting diodes. *Nat. Photon.* **13**, 418–424 (2019).

50. Zhao, L. *et al.* Electrical stress influences the efficiency of $CH_3NH_3PbI_3$ perovskite light emitting devices. *Adv. Mater.* **29**, 1605317 (2017).

51. Cheng, T. *et al.* Ion migration-induced degradation and efficiency roll-off in quasi-2D perovskite light-emitting diodes. *ACS Appl. Mater. Interfaces* **12**, 33004–33013 (2020).

52. Moon, H. & Chae, H. Efficiency enhancement of all-solution-processed inverted-structure green quantum dot light-emitting diodes *via* partial ligand exchange with

thiophenol derivatives having negative dipole moment. *Adv. Opt. Mater.* **8**, 1901314 (2020).

53. Shen, H. *et al.* Visible quantum dot light-emitting diodes with simultaneous high brightness and efficiency. *Nat. Photon.* **13**, 192–197 (2019).

54. Anaya, M. *et al.* Best practices for measuring emerging light-emitting diode technologies. *Nat. Photon.* **13**, 818–821 (2019).

55. Park, M.-H. *et al.* Boosting efficiency in polycrystalline metal halide perovskite light-emitting diodes. *ACS Energy Lett.* **4**, 1134–1149 (2019).

56. Colvin, V. L., Schlamp, M. C. & Alivisatos, A. P. Light-emitting diodes made from cadmium selenide nanocrystals and a semiconducting polymer. *Nature* **370**, 354–357 (1994).

57. Coe, S., Woo, W.-K., Bawendi, M. & Bulović, V. Electroluminescence from single monolayers of nanocrystals in molecular organic devices. *Nature* **420**, 800–802 (2002).

58. Coe-Sullivan, S., Woo, W. K., Steckel, J. S., Bawendi, M. & Bulović, V. Tuning the performance of hybrid organic/inorganic quantum dot light-emitting devices. *Org. Electron.* **4**, 123–130 (2003).

59. Steckel, J. S., Coe-Sullivan, S., Bulović, V. & Bawendi, M. G. 1.3 μm to 1.55 μm tunable electroluminescence from PbSe quantum dots embedded within an organic device. *Adv. Mater.* **15**, 1862–1866 (2003).

60. Steckel, J. S. *et al.* Color-saturated green-emitting QD-LEDs. *Angew. Chem. Int. Ed.* **45**, 5796–5799 (2006).

61. Li, Y., Rizzo, A., Cingolani, R. & Gigli, G. Bright white-light-emitting device from ternary nanocrystal composites. *Adv. Mater.* **18**, 2545–2548 (2006).

62. Anikeeva, P. O., Halpert, J. E., Bawendi, M. G. & Bulović, V. Electroluminescence from a mixed red-green-blue colloidal quantum dot monolayer. *Nano Lett.* **7**, 2196–2200

(2007).

63. Niu, Y. H. *et al.* Improved performance from multilayer quantum dot light-emitting diodes *via* thermal annealing of the quantum dot layer. *Adv. Mater.* **19**, 3371–3376 (2007).

64. Sun, Q. *et al.* Bright, multicoloured light-emitting diodes based on quantum dots. *Nat. Photon.* **1**, 717–722 (2007).

65. Caruge, J. M., Halpert, J. E., Wood, V., Buloví, V. & Bawendi, M. G. Colloidal quantum-dot light-emitting diodes with metal-oxide charge transport layers. *Nat. Photon.* **2**, 247–250 (2008).

66. Kim, L. A. *et al.* Contact printing of quantum dot light-emitting devices. *Nano Lett.* **8**, 4513–4517 (2008).

67. Anikeeva, P. O., Halpert, J. E., Bawendi, M. G. & Bulović, V. Quantum dot light-emitting devices with electroluminescence tunable over the entire visible spectrum. *Nano Lett.* **9**, 2532–2536 (2009).

68. Cho, K.-S. *et al.* High-performance crosslinked colloidal quantum-dot light-emitting diodes. *Nat. Photon.* **3**, 341–345 (2009).

69. Wood, V. *et al.* Air-stable operation of transparent, colloidal quantum dot based LEDs with a unipolar device architecture. *Nano Lett.* **10**, 24–29 (2010).

70. Kim, T. H. *et al.* Full-colour quantum dot displays fabricated by transfer printing. *Nat. Photon.* **5**, 176–182 (2011).

71. Lim, J. *et al.* InP@ZnSeS, core@composition gradient shell quantum dots with enhanced stability. *Chem. Mater.* **23**, 4459–4463 (2011).

72. Kwak, J. *et al.* Bright and efficient full-color colloidal quantum dot light-emitting diodes using an inverted device structure. *Nano Lett.* **12**, 2362–2366 (2012).

73. Kim, H. M., Youn, J. H., Seo, G. J. & Jang, J. Inverted quantum-dot light-emitting diodes

with solution-processed aluminium-zinc oxide as a cathode buffer. *J. Mater. Chem. C* **1**, 1567–1573 (2013).

74. Mashford, B. S. *et al.* High-efficiency quantum-dot light-emitting devices with enhanced charge injection. *Nat. Photon.* **7**, 407–412 (2013).

75. Kim, T. H. *et al.* Heterogeneous stacking of nanodot monolayers by dry pick-and-place transfer and its applications in quantum dot light-emitting diodes. *Nat. Commun.* **4**, 2637 (2013).

76. Lee, K. H. *et al.* Over 40 cd/A efficient green quantum dot electroluminescent device comprising uniquely large-sized quantum dots. *ACS Nano* **8**, 4893–4901 (2014).

77. Dai, X. *et al.* Solution-processed, high-performance light-emitting diodes based on quantum dots. *Nature* **515**, 96–99 (2014).

78. Lim, J. *et al.* Influence of shell thickness on the performance of light-emitting devices based on CdSe/$Zn_{1-x}Cd_xS$ core/shell heterostructured quantum dots. *Adv. Mater.* **26**, 8034–8040 (2014).

79. Yang, Y. *et al.* High-efficiency light-emitting devices based on quantum dots with tailored nanostructures. *Nat. Photon.* **9**, 259–265 (2015).

80. Gong, X. *et al.* Highly efficient quantum dot near-infrared light-emitting diodes. *Nat. Photon.* **10**, 253–257 (2016).

81. Cho, I. *et al.* Multifunctional dendrimer ligands for high-efficiency, solution-processed quantum dot light-emitting diodes. *ACS Nano* **11**, 684–692 (2017).

82. Kim, D. *et al.* Polyethylenimine ethoxylated-mediated all-solution-processed high-performance flexible inverted quantum dot-light-emitting device. *ACS Nano* **11**, 1982–1990 (2017).

83. Xing, Z. *et al.* Inkjet-printed quantum dot light-emitting diodes with an air-stable hole transport material. *ACS Appl. Mater. Interfaces* **9**, 16351–16359 (2017).

84. Li, X. *et al.* Bright colloidal quantum dot light-emitting diodes enabled by efficient chlorination. *Nat. Photon.* **12**, 159–164 (2018).

85. Cao, W. *et al.* Highly stable QLEDs with improved hole injection *via* quantum dot structure tailoring. *Nat. Commun.* **9**, 2608 (2018).

86. Lim, J., Park, Y. S., Wu, K., Yun, H. J. & Klimov, V. I. Droop-free colloidal quantum dot light-emitting diodes. *Nano Lett.* **18**, 6645–6653 (2018).

87. Cao, S. *et al.* Enhancing the performance of quantum dot light-emitting diodes using room-temperature-processed Ga-doped ZnO nanoparticles as the electron transport layer. *ACS Appl. Mater. Interfaces* **9**, 15605–15614 (2017).

88. Li, Y. *et al.* Stoichiometry-controlled InP-based quantum dots: synthesis, photoluminescence, and electroluminescence. *J. Am. Chem. Soc.* **141**, 6448–6452 (2019).

89. Vasilopoulou, M. *et al.* Efficient colloidal quantum dot light-emitting diodes operating in the second near-infrared biological window. *Nat. Photon.* **14**, 50–56 (2020).

90. Li, X. *et al.* Quantum□dot light□emitting diodes for outdoor displays with high stability at high brightness. *Adv. Opt. Mater.* **8**, 1901145 (2020).

91. Won, Y.-H. *et al.* Highly efficient and stable InP/ZnSe/ZnS quantum dot light-emitting diodes. *Nature* **575**, 634–638 (2019).

92. Lin, J. *et al.* High□performance quantum□dot light□emitting diodes using NiO_x hole□injection layers with a high and stable work function. *Adv. Funct. Mater.* **30**, 1907265 (2020).

93. Liu, D. *et al.* Highly stable red quantum dot light-emitting diodes with long T_{95} operation lifetimes. *J. Phys. Chem. Lett.* **11**, 3111–3115 (2020).

94. Xiang, C. *et al.* High efficiency and stability of ink-jet printed quantum dot light emitting diodes. *Nat. Commun.* **11**, 1646 (2020).

95. Chen, D. *et al.* Shelf-stable quantum-dot light-emitting diodes with high operational performance. arXiv:2005.10735 (2020).